Journal of Materials Chemistry A

Chemomechanical Behaviors of Layered Cathode Materials in Alkali Metal Ion Batteries

Journal:	*Journal of Materials Chemistry A*
Manuscript ID	TA-REV-07-2018-006875.R1
Article Type:	Review Article
Date Submitted by the Author:	17-Sep-2018
Complete List of Authors:	Xu, Zhengrui; Virginia Polytechnic Institute and State University, Chemistry Rahman, Muhammad; Virginia Polytechnic Institute and State University, Chemistry Mu, Linqin; Virginia Polytechnic Institute and State University, Chemistry Liu, Yijin; Stanford Synchrotron Radiation Lightsource Lin, Feng; Virginia Polytechnic Institute and State University, Chemistry

Chemomechanical Behaviors of Layered Cathode Materials in Alkali Metal Ion Batteries

Zhengrui Xu,[1] Muhammad Mominur Rahman,[1] Linqin Mu,[1] Yijin Liu,[2] Feng Lin[1]*

1. Department of Chemistry, Virginia Tech, Blacksburg, VA 24061, USA
2. Stanford Synchrotron Radiation Lightsource, SLAC National Accelerator Laboratory, Menlo Park, CA 94025, USA

*Email: fenglin@vt.edu

Abstract

Layered cathode materials (LCMs), because of their high energy density and relatively stable performance, represent an important class of cathode materials for alkali metal ion (e.g., Li^+, Na^+) batteries. Chemomechanical behaviors of LCMs, which affect battery performance dramatically, have drawn extensive investigations in recent years. Most chemomechanical processes have some common chemical and structural origins that are in the center of materials chemistry, for example, defects and local bonding environments in the solid state. In this review, we first discuss the chemomechanical breakdown of LCMs by introducing their categories and negative effects on the battery performance. We then systematically analyze factors that govern the initiation and propagation of chemomechanical breakdown and summarize their formation mechanisms. Strategies that can enhance the chemomechanical properties of LCMs or reduce the destructive effects of chemomechanical breakdown are then discussed. Finally, light is brought onto the new state-of-the-art techniques that have been applied to study chemomechanical breakdown. This review virtually includes most aspects of the chemomechanical behaviors of LCMs and provides some insights into the important chemical motifs that determine the chemomechanical properties. Therefore, we believe that advanced design protocols of LCMs can be developed to effectively address the chemomechanical breakdown issue of LCMs.

Keywords: layered cathode, chemomechanical, crack, surface, grain boundary

1. Introduction

In order to ensure a green and pollution-free future, harvesting energy from sustainable resources along with shifting from gasoline-powered vehicles to electric vehicles (EVs)[1] are of prime importance. To achieve these two goals, it is crucial to develop grid-scale energy storage systems and EVs[2]. A promising energy storage candidate for grids and EVs is alkali metal ion batteries (e.g., lithium-ion batteries, LIBs). LIBs have been widely used in portable electronics because of their high energy density, high power density, superior safety features, and long cycle life[3]. However, LIBs cannot satisfy the increasing performance requirements for modern portable electronics, EVs, and grid-scale energy storage systems. We have witnessed the impressive progress in integrated circuits (ICs) in the past 50 years, which has almost followed the Moore's law[4] that the number of transistors per square inch doubles every 18 months. More transistors means faster processing capability and consequently more energy consumption. However, the performance of the power provider (LIBs) is lagging far behind. We also witnessed the exciting progress in harvesting different forms of sustainable energy, such as wind energy[5,6], solar energy[7,8], hydropower energy[9], biomass energy[10,11], and marine energy[12]. Nevertheless, the aforementioned sustainable energy resources have the same intrinsic drawbacks: intermittency and unpredictable fluctuations. Integrating those fluctuating green energy is a huge challenge to the modern grid[13]. Storing renewable energy is therefore vital for practical applications[14].

To further enhance the performance of LIBs, we need better understanding of their fading mechanisms. Chemomechanical breakdown (i.e., formation of cracks), one of the main

fading mechanisms of LIBs, has been widely observed in the anode, solid electrolyte interphase (SEI), and cathode. Strategies to inhibit chemomechanical breakdown of anode materials include reducing the particle size[15,16,17], surface engineering[18], and advanced nanostructure design[19,20]. Readers can refer to some recent reviews about the chemomechanical breakdown of anode materials[21,22,23]. To resolve the chemomechanical breakdown problems in SEI, self-healing SEI[24], artificial SEI[25,26,27], and electrolyte additives[28] were proposed. In contrast, the chemomechanical behaviors of the cathode are much more complicated. Many different categories of cathode materials have been proposed in the past three decades[29]. Among which, LCMs[30,31] are considered as one class of the most promising cathodes, due to their high energy density, high power density, and good cycling stability. Many factors are responsible for the capacity fading in LCMs[32], such as phase transformations from the layered structure to the rock-salt and/or spinel structure[33], undesired cathode–electrolyte side reactions[3,34], lattice oxygen release[35,36], transition metal dissolution[37], and chemomechanical breakdown[38,39,40]. However, by no means can this review cover all of these factors. We specifically highlight the chemomechanical breakdown of LCMs in this review.

To improve the volumetric energy density and stability of LCMs (e.g., $LiNi_xMn_yCo_{1-x-y}O_2$, NMC), most studies aim to form micron-sized spherical polycrystalline particles consisting of nano-sized single crystals[38,39,41,42,43]. In addition, great effort has been made to push the charge cut-off voltage higher than 4.5 V (all voltages in this paper are against Li/Li^+) to reach the capacity that is close to the theoretical limitation[38,44]. Therefore, the chemomechanical breakdown of LCM polycrystalline particles can occur due to the random orientation of the single crystals, anisotropic volume expansion/contraction, electrolyte infiltration, lattice oxygen release, and heterogeneous phase transformations.

Chemomechanical breakdown of the cathode leads to the detachment of active particles from the nearby active particles, conductive carbon matrices, and current collector. The detachment can lead to reduced electronic conductivity[40] and loss of effective active particles[45]. Moreover, cracked cathode particles have a larger surface area because the cracks expose the intact bulk[41]. The increased surface area and electrolyte penetration result in more undesired cathode–electrolyte side reactions[3,34] and accelerated transition metal dissolution[46,47]. Thus, the formation of cracks imposes negative effects on the battery performance. The formation of cracks is governed by different factors, and here we categorize the factors as intrinsic and extrinsic factors. The intrinsic factors are related to the cathode itself, such as the cathode composition[41,44] and particle size[48,49]. The extrinsic factors are associated with charging and discharging conditions, and examples are depth of charge/discharge[50], cycling-rate[51,52], and cycle number[40,53]. Cracking has been intensively observed, yet its formation mechanisms have not been completely understood. Evolution of crystal structure can introduce volume change and subsequent microstrain in the particles[54], and when the strain reaches a certain level, it will be released through the formation of cracks. Defects (e.g., dislocations) inside the primary particles can propagate and lead to the formation of intragranular cracks[38]. Moreover, release of lattice oxygen reduces the stability of the cathode and is partially responsible for the formation of intragranular and intergranular cracks[35,36]. Equipped with the knowledge of crack formation, some strategies have been designed to mitigate cracking or reduce the negative effects of cracks. Among those strategies, surface engineering has been shown the most common and effective one[55]. Other strategies, such as grain engineering[56], elemental substitution[57], pre-cycling treatment[58,59], reducing particle size[60], and electrolyte additives[61] are also covered in this review. Chemomechanical breakdown of the LCMs for sodium-ion batteries (SIBs) are compared with that in LIBs.[62,63]

Finally, some recently developed analytical techniques[49,64,65] are reviewed to enlighten the methodology for studying the chemomechanical properties of LCMs. The purpose of this review is to summarize the recent progress in characterizing, understanding, and modifying the chemomechanical properties of LCMs, with an emphasis on the LCMs for LIBs.

2. Categories of cracks and their impact on battery performance

The LCMs are designed to have spherical morphology for the relatively small surface area. Secondary particles of LCMs consist of densely packed single crystals (i.e. primary particles) with mostly random orientations (Fig. 1 (a)[39]). An exception is that $LiCoO_2$ (LCO), one of the LCMs, has large single crystals[66]. Such structural design can enhance its volumetric density and alleviate cathode–electrolyte side reactions because of the relatively small surface area. However, this structural design has an unresolved problem: during the charging and discharging process, formation of cracks can occur inside and between primary particles, which can then increase the surface area of the cathode and induce more side reactions relative to those intact particles.

Based on the physical location, cracks can be divided into two main categories: intragranular cracks and intergranular cracks, the former occurs within the primary particles[38,41,42,43], whereas the latter occurs between the primary particles (usually along grain boundaries)[39]. Intragranular cracks are usually caused by the loss of several transition metal layers[38]. The dark straight lines, pointed by the yellow arrows in Fig. 1 (b)[38], are intragranular cracks in a $LiNi_{1/3}Mn_{1/3}Co_{1/3}O_2$ (NMC333) material. It is evident that intragranular cracks are inside a primary particle, and their length ranges from tens to hundreds of nanometers. Intragranular cracks are widely observed in LCMs, such as in NMC333[38], LCO[67], $LiNi_{0.6}Mn_{0.2}Co_{0.2}O_2$ (NMC622)[68], and even in olivine-type cathode materials such as $LiFePO_4$ (LFP)[69]. Although it is challenging to quantify the negative impact of intragranular

cracks, it ultimately leads to the formation of large cracks that act similar to intergranular cracks. The density of intragranular cracks is usually orders of magnitude higher than that of intergranular cracks[70]. Intergranular cracks form between the primary particles, and usually along grain boundaries[35]. Fig. 1 (c)[41] shows the intergranular cracks (irregular void regions inside the secondary particle) in Ni-rich NMC material. Intergranular cracks have a much larger size comparing to intragranular cracks. Intergranular cracks are also widely reported in LCMs, for example, $LiNi_{0.8}Co_{0.15}Al_{0.05}O_2$ (NCA)[40], $LiNiO_2$ (LNO)[50], NMC333[71], and olivine-type LFP[72,73].

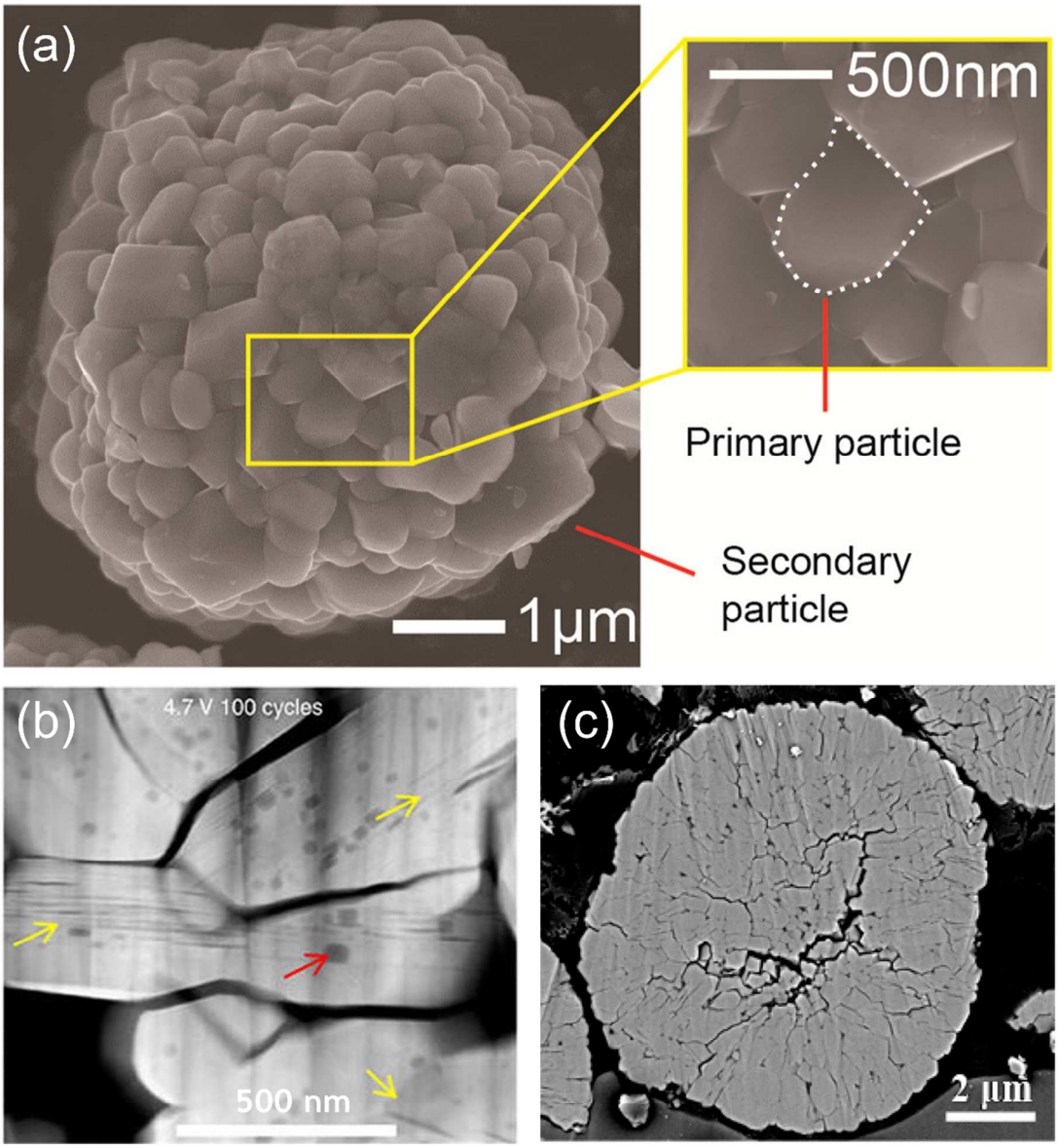

Fig. 1 (a) Illustration of primary and secondary particles: scanning electron microscopy (SEM) of uncycled NCA primary and secondary particles[39]. (b) An example of intragranular cracks: low magnification high-angle annular dark-field (HAADF) images of NMC333 (after 100 cycles at 4.7 V cut-off voltage), showing the intragranular cracks (yellow arrows) inside the primary particles[38]. (c) An example of intergranular cracks: cross-sectional SEM image of the $Li_{1-\delta}Ni_{0.95}Co_yMn_{0.05-y}O_2$ cathode particle (first fully charged state at 4.3 V cut-off voltage)[41].

Used with permission from ref. 39, 38, and 41.

The formation of intragranular and intergranular cracks is inevitable in most LCMs, and their occurrence commonly accompanies with decreased electrochemical performance. Four main negative impacts are included in this review (Fig. 2): poor electronic conductivity, loss of active material, more severe cathode–electrolyte side reactions, and dissolution of transition metals. The four main negative effects are not independent to each other and the electrochemical performances of LIBs are compromised by the synergistic effect of the four negative impacts.

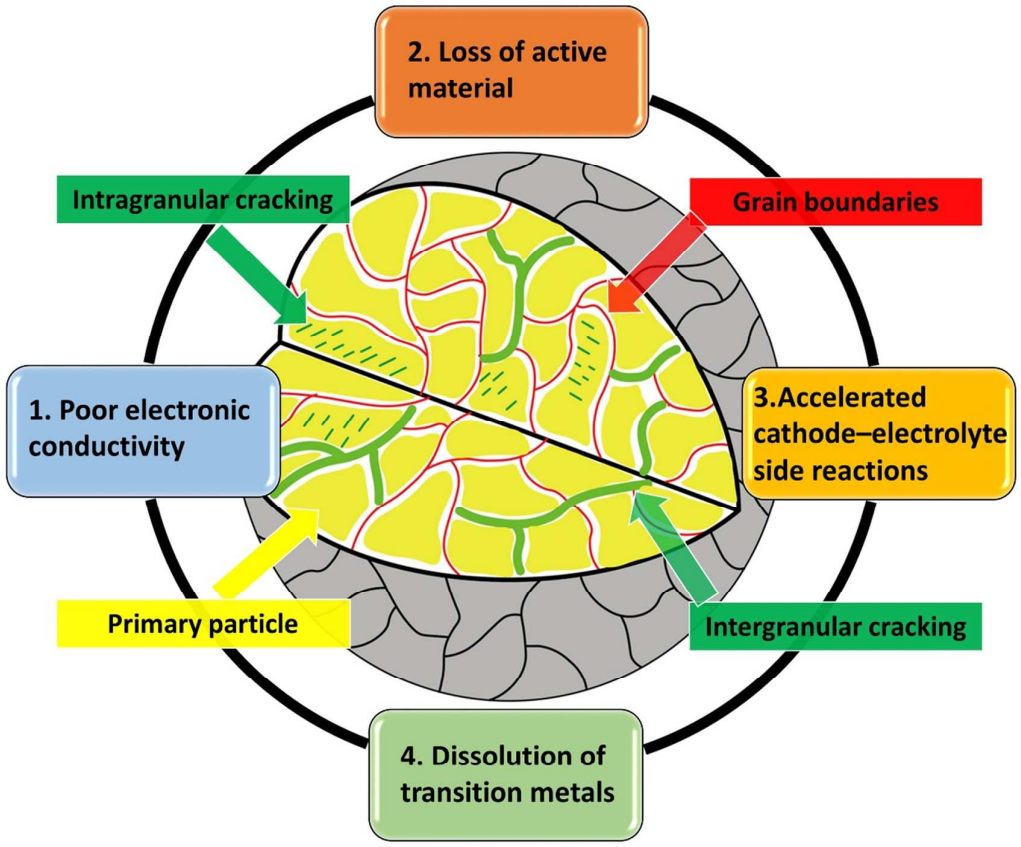

Fig. 2 Schematic representation of the four negative impacts induced by intragranular and intergranular cracks. The irregular yellow regions stand for primary particles and the red lines stand for grain boundaries. Primary particles have random orientations and they packed

tightly to form the secondary particle. The green stripes inside the primary particles are intragranular cracks, while the green gaps between primary particles are intergranular cracks.

Poor electronic conductivity

During charging process, electrons in the cathode material move across primary cathode particles and then travel to the anode through the external circuit. Intergranular cracks in cathode particles can lead to the detachment of the active material from the nearby active material, conductive carbon black, and current collector, which is responsible for the inferior electronic conductivity. The reduced electronic conductivity leads to dramatic increment of R_{ct} (charge-transfer kinetic resistance), which is considered as an important factor for significant capacity drop.[40,74,75]

The inferior electronic conductivity can further lead to state-of-charge (SOC) heterogeneity in individual particles. SOC heterogeneity means the non-uniform oxidation state distribution of a transition metal (e.g., Ni)[76], which accounts for accelerated crack formation[49,77]. Liquid electrolyte is a good Li ion conductor but not an electron conductor, while the solid cathode particles can conduct both electrons and Li ions. This means Li ions can diffuse through the cathode and electrolyte, while electrons can only be conducted through the solid cathode. Before cracking, the Li ions and electrons at the same spot share the same geometrically optimal pathway (Fig. 3 (a) green lines). Therefore, there is no path length differences between the Li ions and electrons at the same physical site. On the contrary, cracking and electrolyte infiltration induce the path length difference between the Li ions and electrons. During the charging process, the Li ions diffuse to the surface of solid cathode, and then be conducted through the liquid electrolyte, which possesses higher Li ion conductivity than the solid cathode. When the electrolyte penetrates the cracked cathode particles, it reduces the path length of Li ions that are inside the particles (Fig. 3 (a) blue lines).

Meanwhile, the cracks generally increase the path length of electrons. Cracks are physical barriers to electrons, which means the electrons need to detour and travel longer distance to reach the surface (Fig. 3 (a) red lines). The path length difference between the electrons and Li ions at different spot can be calculated and the result is shown in Fig. 3 (b). Intergranular cracks lead to different degrees of path length difference based on the geometry of cracks and electrolyte infiltration effect. Moreover, the difference in the diffusion time of Li ions and electrons lead to charge heterogeneity at the secondary particle level. The electrons in the cathode particle need to move to the surface during charging process, and after crack formation (Fig. 3 (c)), different regions of the surface have different electron traffic because of the electron detour effect (Fig. 3 (d)). Recently, Tian et. al observed charge heterogeneity for NMC622 particles after electrochemical delithiation (Fig. 3 (e))[76]. The inhomogeneous Ni oxidation states were partially due to the disruption of electronic wiring and subsequent particle isolation.

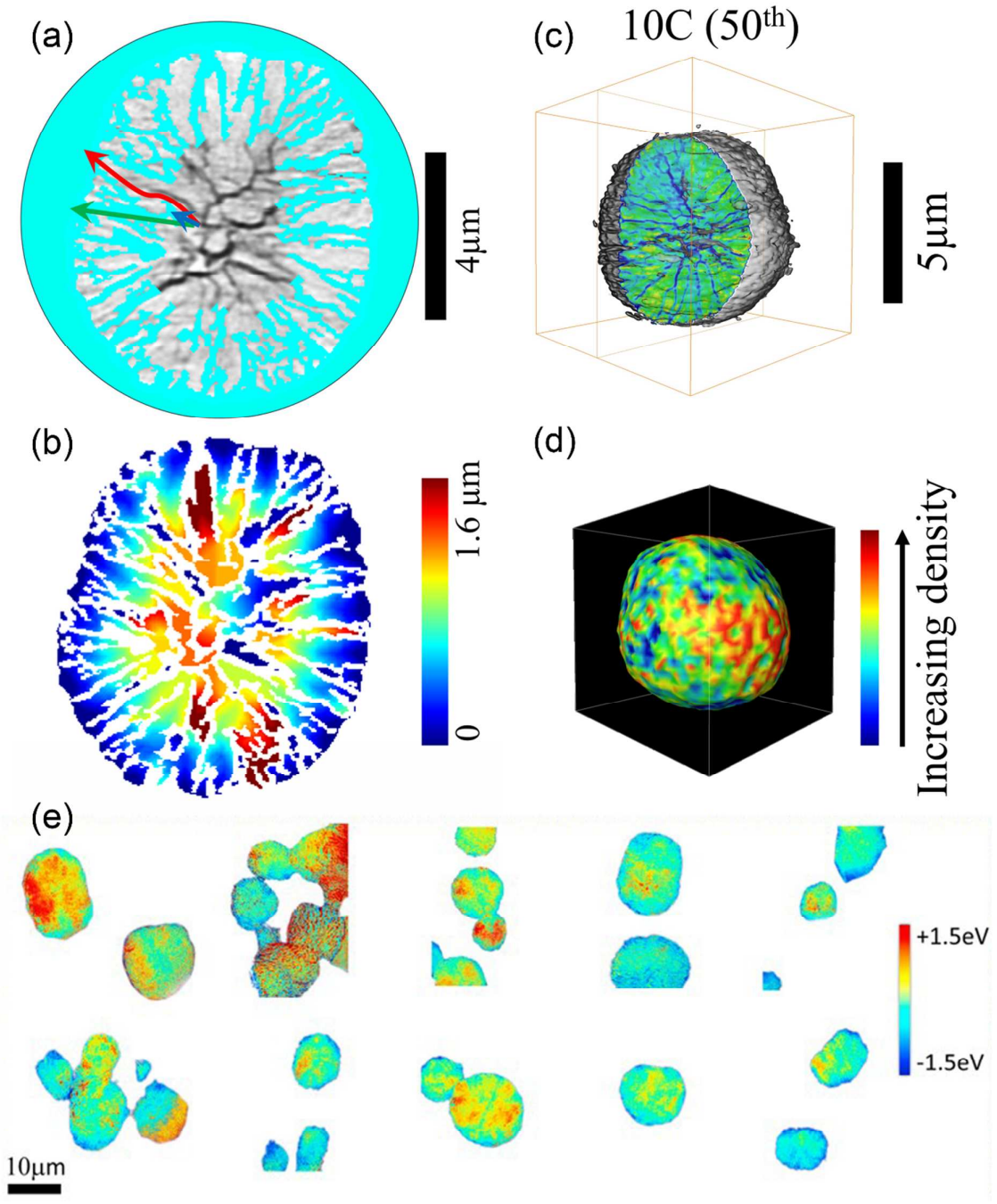

Fig. 3 (a-b) Simulation of the electrolyte infiltration effect. (a) Schematic representation of the diffusion pathways for: electrons and Li ions before the crack formation (green lines), electrons after crack formation (red lines), and Li ions after crack formation (blue lines). The gray domains are cathode materials, the void regions between cathode materials are

intergranular cracks, and the cyan background is the liquid electrolyte. (b) Color map showing the path length difference between Li ions and electrons induced by cracking and electrolyte infiltration. The path length difference is calculated by subtracting the path length of Li ions from that of electrons at the same spot. Blue represents small difference and red means large difference. (c) 3D rendering of the NMC622 particle that has been cycled for 50 times at 10 C. (d) Traffic load (the number of electrons passing through a specific surface area) map of the particle in (c).[49] (e) Color mapping of Ni oxidation state heterogeneity of electrochemically charged NMC622 electrode, where blue represents low oxidation state and red indicates high oxidation state[76]. Used with permission from ref. 49 and 76.

Loss of active material

Disconnection in LCMs, induced by intergranular cracks, can lead to etched surface after cycling (Fig. 4 (a) and (b)), and part of the etched surface will further separate from the bulk region and form fragmented pieces (Fig. 4 (c)). The fragmented pieces are "dead regions" of the cathode for two reasons. One is that once the fragmented pieces detach from the bulk region, the electrons in fragmented pieces cannot reach the surrounding conductive matrices. The fragmented pieces thus cannot contribute to the electrochemical reaction anymore. The other reason is that Mn ions in the fragmented pieces are permanently reduced from Mn^{4+} to Mn^{2+}, most likely in forms of redox inactive rock-salt phases. Electron energy loss spectroscopy (EELS) spectra (Fig. 4 (c), (d), and (e)) indeed show that Mn ions in the fragmented pieces were Mn^{2+}, while the Mn ions in the bulk were Mn^{4+}. The "dead regions" cannot intercalate or de-intercalate Li ions anymore, which is partially responsible for capacity fading.

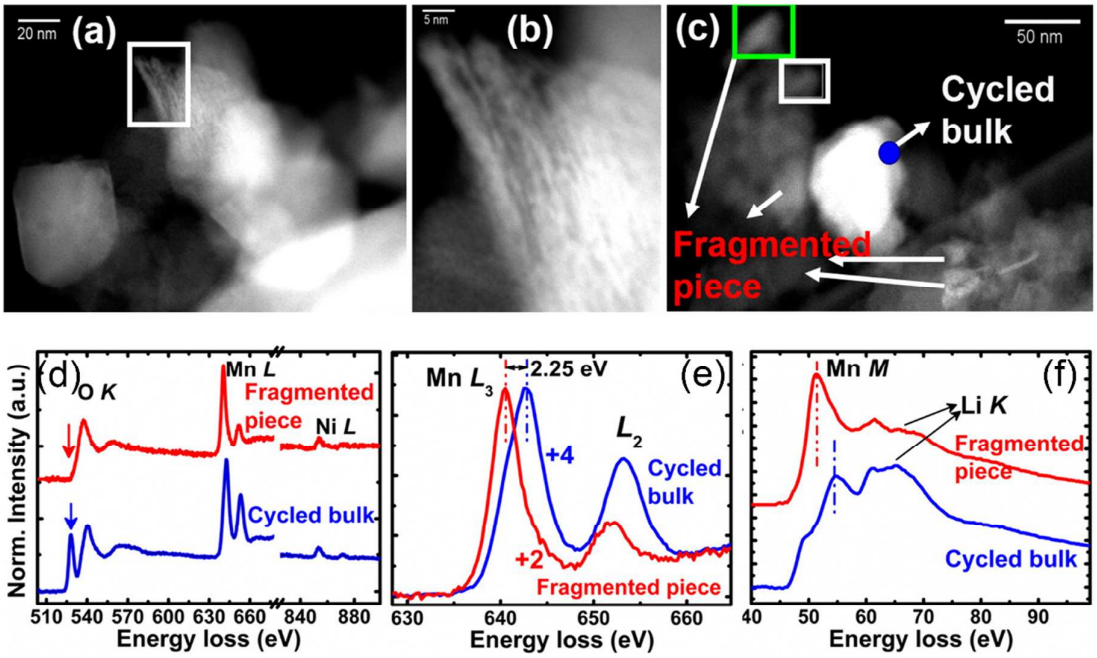

Fig. 4 (a-c) Etched surface of $Li[Li_{0.2}Ni_{0.2}Mn_{0.6}]O_2$ cathode after cycling. (a) Overview image of the surface after cycling. (b) Zoomed-in image of the white rectangle region in (a). (c) Overview image of fragmented pieces and cycled bulk of the cathode. (d-f) EELS results of cycled bulk (blue) and fragmented pieces (red): (d) O K, Mn L, and Ni L edges, (e) Mn L edge, and (f) Mn M and Li K edges.[45] Used with permission from ref. 45.

Accelerated cathode–electrolyte side reactions

Secondary particles of LCMs are designed to have spherical morphology to reduce their specific surface area. Intergranular cracks can produce fresh surfaces and expose the formerly intact grain boundaries to the liquid electrolyte. The fresh surfaces can react with the liquid electrolyte and form more surface reconstruction layers. Surface reconstruction layers are electrochemically inactive with relatively inferior ion conductivity, which partially accounts for the resistance buildup and capacity fading in LIBs[40,41]. Surface reconstruction involves the structural change from a R-3m layered structure to a Fm-3m rock-salt (Fig. 5)

and it has been intensively observed for LCMs[33,78,79,80], including stoichiometric layered materials and Li/Mn-rich layered oxides. The degraded surface layer form instantly after the cathode particles are soaked in liquid electrolyte, and its thickness can increase after cycling. This proves that the surface reconstruction process involves both cathode–electrolyte reactivity and electrochemical activation.[33] Moreover, the surface construction predominantly occurs along the Li-diffusion direction, and examples include $LiNi_{0.4}Mn_{0.4}Co_{0.2}O_2$ (NMC442) (Fig. 5 (a))[33] and Li/Mn-rich layered oxides (Fig. 5 (b))[78]. The surface reconstruction is mainly induced by lattice oxygen release and the preferential migration of Mn and Ni ions [79]. It was observed that the removal of Li ions accompanies with the loss of lattice oxygen ions at the surface. As a result, some surface transition metal ions only coordinate with five oxygen ions, and the destabilized transition metals will then move to the empty Li sites and form the rock-salt structure. When Mn ions migrate to the bulk, the Mn-to-Ni ratio increase from the surface to the bulk, as shown in Fig. 5 (c)[79].

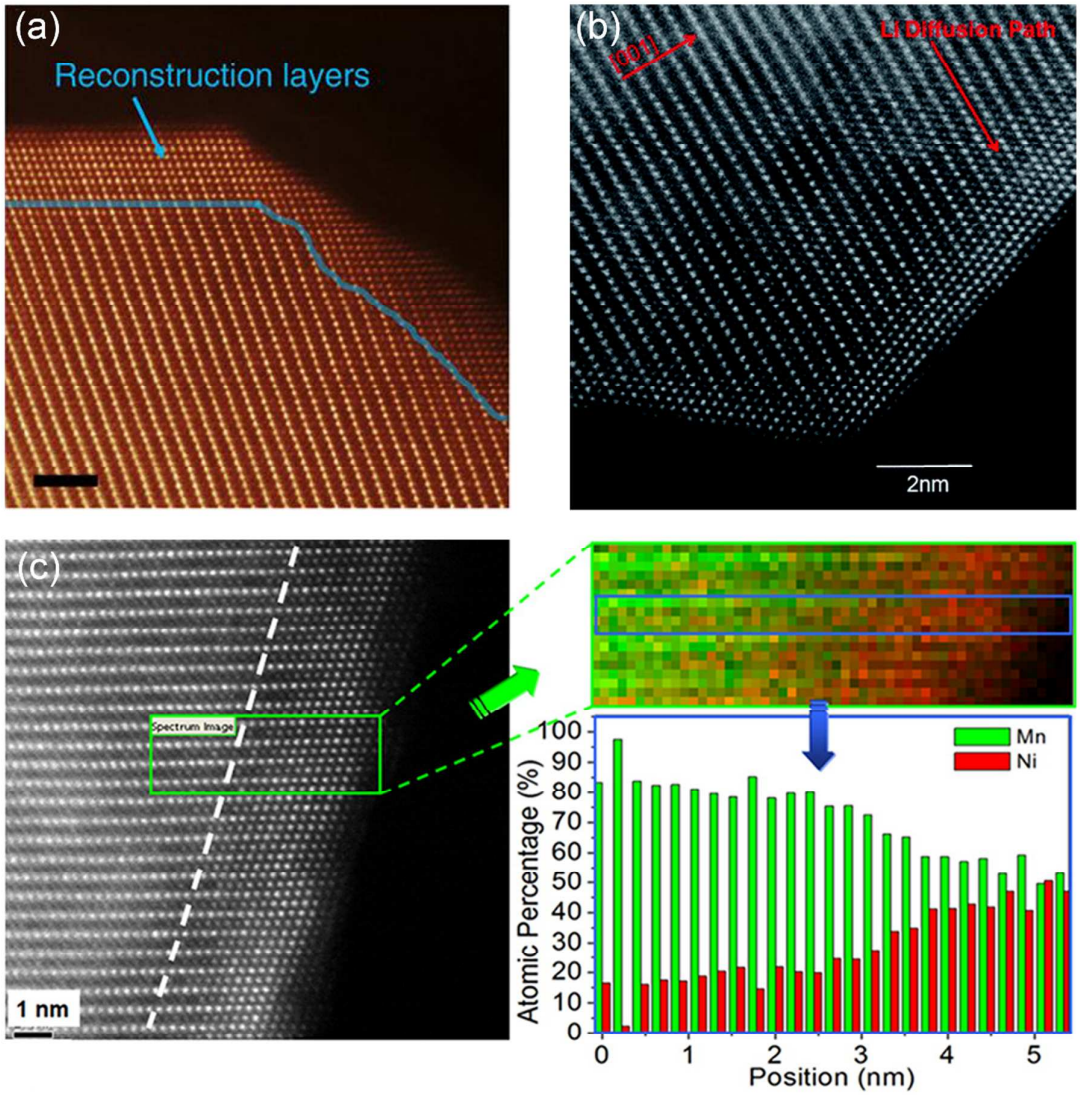

239

240 Fig. 5 (a) Observation of surface reconstruction layers of NMC442 particles (after 1 cycle,
241 2.0-4.7 V) with annular dark-field scanning transmission electron microscopy (ADF-STEM).
242 The scale bar is 2 nm.[33] (b) The surface reconstruction layers in cycled Li/Mn-rich
243 $Li[Ni_{1/5}Li_{1/5}Mn_{3/5}]O_2$.[78] (c) The surface reconstruction layers, chemical maps, and evolution
244 of the Mn and Ni atomic concentration in Li/Mn-rich $Li_{1.2}Mn_{0.61}Ni_{0.18}Mg_{0.01}O_2$ (after 50
245 cycles under C/2).[79] Used with permission from ref. 33, 78, and 79.

Dissolution of transition metals

The dissolution of transition metals, such as Ni, Co, and Mn, is more severe after chemomechanical breakdown. Among the three aforementioned transition metals, the dissolution of Mn ions was reported to be the easiest[46,47] and it can occur through two possible mechanisms. The first mechanism is the Mn^{3+} disproportion reaction according to the $2Mn^{3+} \rightarrow Mn^{2+} + Mn^{4+}$ route[81,82]. The second mechanism is the HF attack on cathode[83,84]. $LiPF_6$, a common component of the liquid electrolyte, decomposes easily as $LiPF_6 \rightarrow LiF + PF_5$. With trace of water, PF_5 can further decompose as $PF_5 + H_2O \rightarrow 2HF + POF_3$[84]. HF can then react with the cathode, leading to the dissolution of transition metals. Moreover, H_2O is another product from the cathode–HF reaction, and H_2O promotes the decomposition of PF_5 and produce more HF, which makes the transition metal dissolution reaction auto-catalytic[85]. The dissolution of Mn ions has two main negative impacts. Mn ions dissolved in the electrolyte can re-deposit on the cathode surface[86], which induces a resistive layer for electrons and Li ions. The dissolved Mn ions can also migrate to the anode surface through the electrolyte[87] and interrupt the SEI layer[88]. Transition metals deposited on the anode work as catalysts for the decomposition of SEI components, which leads to the formation of inactive layer on the anode surface and cracks in the SEI layer[88]. The decomposition of $(CH_2OCO_2Li)_2$ (one of the SEI components) promotes the formation of Li_2CO_3, which can react with $LiPF_6$ to produce LiF and CO_2[89]. Moreover, the decomposition of $(CH_2OCO_2Li)_2$ can induce some cracks in the SEI, and the cracks contribute to more SEI formation. As a result, the dissolution of transition metals interrupts the SEI layer and induces more SEI formation, which lead to decreased electrochemical performance.

The dissolution of Co ions is widely observed in Co containing cathode materials[90,57], though it is not dominant. Moreover, the dissolution of Ni ions from the surface

usually accompanies the surface transformation from layered structure to spinel and/or rock-salt structure. Although the dissolution of Ni is not dominant, it can be accelerated by high Ni-content, high cut-off voltage, and elevated temperature[37]. An example is that the degree of Ni dissolution in $LiNi_{0.9}Mn_{0.05}Co_{0.05}O_2$ is an order of magnitude higher than that in NMC622[44]. Interestingly, the dissolution of Co and Mn ions is also more severe in high Ni-content samples. Even though the Co and Mn concentration in $LiNi_{0.9}Mn_{0.05}Co_{0.05}O_2$ is only one-fourth of that in NMC622[44], the dissolution of Co and Mn ions are much more obvious in the former. The possible reason is that $LiNi_{0.9}Mn_{0.05}Co_{0.05}O_2$ has more cracks, which provide channels for electrolyte infiltration and induce more cathode–electrolyte reactions.

3. Factors affecting the crack formation and crack formation mechanisms:

Even though how intriguing the phenomenon of crack formation can be, there are limited number of reports on the formation mechanisms of cracks. The factors affecting the crack formation can be traced down to intrinsic and extrinsic factors. Intrinsic factors mainly relate to the properties of cathode particles. To the best of our knowledge, Ni-content and particle size are reported to affect the formation of cracks. Extrinsic factors can be referred to charging and discharging conditions, such as state of charge, cycling rate, and cycle number. Intrinsic and extrinsic factors affect crack formation mainly based on three different mechanisms: evolution of crystal structure, propogation of defects (e.g., dislocations), and lattice oxygen release.

3.1 Intrinsic factors:

Ni-content

Undesired side reactions, such as surface reconstruction and transition metal

dissolution, are more severe in Ni-rich materials ($LiNi_xMn_yCo_{1-x-y}O_2$, $x > 0.8$). Ni-rich materials[41,91,92,93,94] have more severe phase transition near the end of charge, which leads to a higher extent of anisotropic volume change and produces more freshly exposed surface area. The severe anisotropic volume change, however, can be suppressed when x (the Ni-content) is less than 0.8 (Fig. 6 (a)). At the beginning of charging process, the c axis of samples with different Ni-content expands the same length. However, near the charging end, the c axis of NMC622 shrink only 2.6 %, while $LiNi_{0.95}Co_{0.025}Mn_{0.025}O_2$ shrink by 6.9 % in the c axis (Fig. 6 (b)). This dramatic difference accounts for the larger size and higher density of cracks in Ni-rich samples. The cracks in the Ni-rich sample, indicated by the red lines in Fig. 6 (a), provide more channels for electrolyte infiltration. Fresh cathode surfaces can then react with electrolyte and form NiO-like layers at the surface and in the interior of cathode particles. The NiO-like layer can impede Li ion diffusion and lead to impedance increment (Fig. 6 (c)). Higher Ni-content can enhance the initial discharge capacity, however, it deteriorates the stability of NMC material, as shown in Fig. 6 (d). NMC622 had an initial capacity around 180 mAh/g at 0.5 C, and the capacity retention was 96.5% after 100 cycles, whereas the initial capacity of LNO was around 230 mAh/g at 0.5 C and the capacity retention was only 74.9% after 100 cycles.

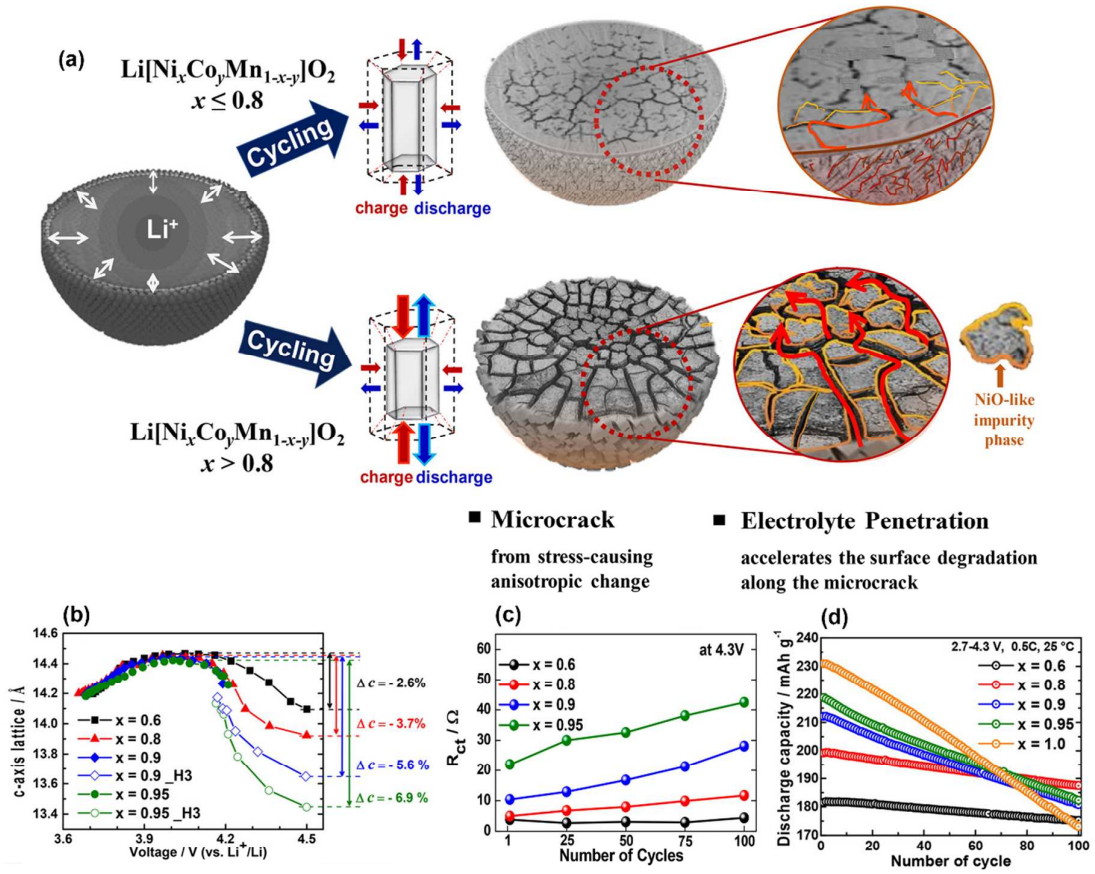

311

312 Fig. 6 (a) Schematic figure showing the capacity fading mechanism of Ni-rich NMC cathodes.
313 Higher Ni-content results in higher extent of anisotropic volume change and subsequently
314 more cracks in the cathode particles. More and larger cracks provide more channels for
315 electrolyte infiltration, which leads to more severe surface degradation. Evolution of (b)
316 c-axis lattice parameter, (c) charge transfer resistance, and (d) discharge capacity of Ni-rich
317 NMC materials with different Ni-content (x = 0.6, 0.8, 0.9, 0.95, and 1).[41] Used with
318 permission from ref. 41.

319 In addition to more crack formation for higher Ni-content samples, it also leads to
320 thicker surface degradation layers. A comparison between NMC622 and
321 $LiNi_{0.90}Co_{0.05}Mn_{0.05}O_2$[44] depicts that increasing the Ni-content in NMC leads to thicker

NiO-like surface degradation layer. Fig. 7 (a) and (b) are the transmission electron microscopy (TEM) images for NMC622 with a cut-off voltage of 4.3 V and 4.5 V, respectively. The thickness of the surface degradation layer is about 3 nm. By increasing the Ni-content to 0.9, the surface degradation layer increases and a thin amorphous layer also forms above the NiO-like rock-salt structure layer. As seen in Fig. 7 (c) and (d), the surface degradation layer is about 5 nm for $LiNi_{0.90}Co_{0.05}Mn_{0.05}O_2$ with a cut-off voltage of 4.3 V and 4.5 V, respectively. The amorphous layer is formed by the release of oxygen.

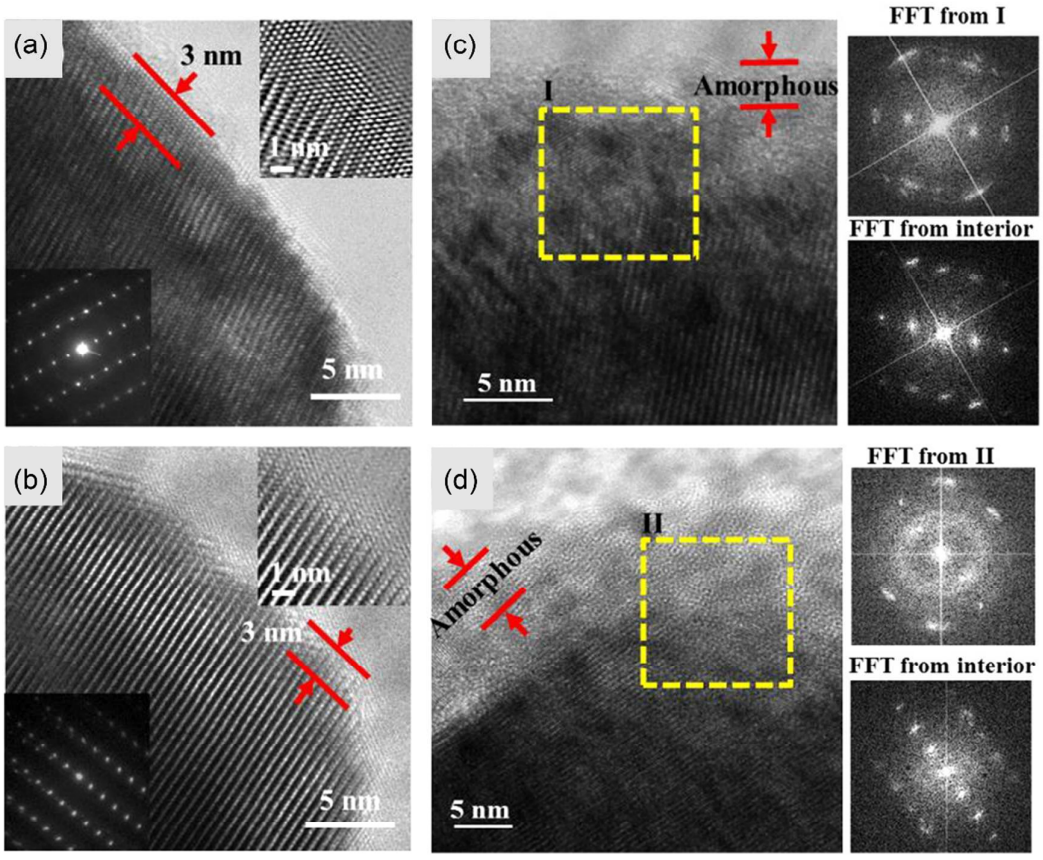

Fig. 7 Comparison of surface degradation layers in NMC622 and $LiNi_{0.90}Co_{0.05}Mn_{0.05}O_2$ at different cut-off voltages based on TEM images. TEM images of NMC622 charged to (a) 4.3 V and (b) 4.5 V. TEM images and Fourier transform of $LiNi_{0.90}Co_{0.05}Mn_{0.05}O_2$ charged to (c)

4.3 V and 4.5 V.[44] Used with permission from ref. 44.

Particle size

Particle size, including primary and secondary particle sizes, is thought to be another intrinsic factor that affects the formation of cracks. Our recent study[49] shows that the size of secondary particles positively correlates with the degree of cracking, as attested by the transmission X-ray microscopy (TXM) data (Fig. 8 (a) and (b)). Obviously small particles are more robust against crack formation, however, nano-sized secondary particle design cannot be adopted for practical cathodes, because nano-sized secondary particle has inferior packing density[48] and more severe cathode–electrolyte reactions. The reason why larger secondary particle leads to more cracks has not been understood yet. The consensus among material scientists is that micro-fracture in ceramics can be suppressed if the grain size is under a material-specific size.[95] With an analytical micromechanical model, Chiang[60] and coworkers showed that when the primary particle size is smaller than some critical value, grain boundary micro-fracture formation in LCMs would be suppressed. Fig. 8 (c) shows the critical sizes for LCO, NCA, and NMC, under which micro-fracture will not grow.

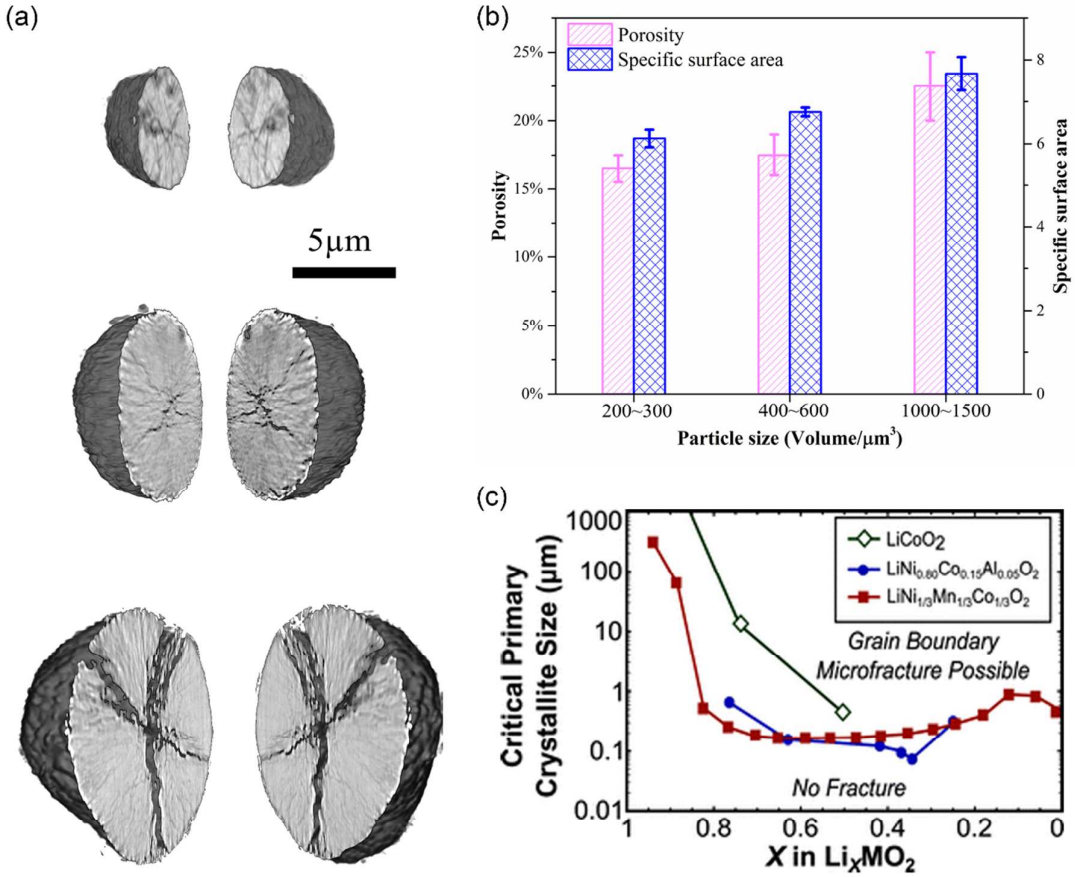

Fig. 8 (a) Visualization of crack formation in NMC secondary particles of different sizes. All the particles were cycled at 10 C for 50 times. (b) Quantification of the porosity and the specific crack surface area of particles in (a).[49] (c) SOC-dependent critical sizes for selected LCMs[60]. Used with permission from ref. 49 and 60.

3.2 Extrinsic factors:

State of charge

During the charging process, Li ions de-intercalate from the cathode and intercalate into the anode. Charging the cathode to higher voltage can extract more Li ions from the cathode and deliver higher discharge capacity[96]. However, higher cut-off voltage correlates to

more phase transformation processes and subsequently more crack formation. The phase transformation process will be discussed in detail later.

LNO particles remain intact when they are cycled at low cut-off voltage (4.1 V), as shown in Fig. 9 (a) and (d). When increasing the cut-off voltage to 4.2 V, crack formation becomes obvious (Fig. 9 (b) and (e)). Moreover, if the cut-off voltage reaches 4.3 V, the crack formation increase dramatically, as seen in Fig. 9 (c) and (f).[50] The underlying mechanism for such observation is the phase transformation process under high cut-off voltage, which can generate mechanical strains and accelerate the formation of micro-cracks[57]. The dQ/dV plot of the samples with different cut-off voltage is shown in Fig. 9 (g), (h), and (i). The repeated H2 → H3 phase transition[44,97] at 4.15 V is considered as the primary factor that causes crack formation. Capacity fading can be mitigated by limiting the cut-off voltage of LNO to 4.1 V. In addition, higher cut-off voltage leads to more severe crack formation is also observed in NMC materials.[75,98]

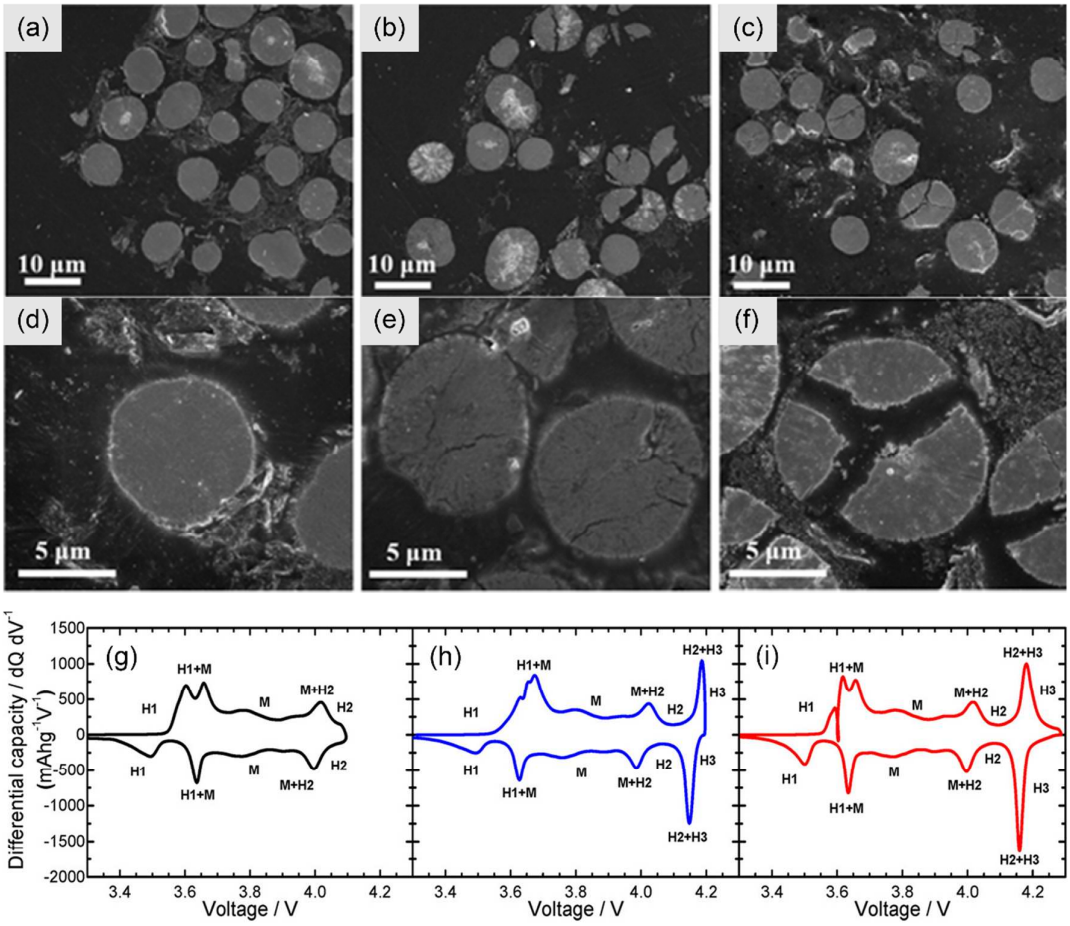

Fig. 9 Cross-sectional SEM images of the first charged LNO cathode at (a) and (d) 4.1 V, (b) and (e) 4.2 V, and (c) and (f) 4.3 V. The dQ/dV curves from the initial charge and discharge curves at upper cutoff voltages of (g) 4.1 V, (h) 4.2 V, and (i) 4.3 V.[50] Used with permission from ref. 50.

Cycling-rate

Fast charging and discharging capability is an important parameter for practical batteries, especially for those designed for EVs. Fast charging and discharging is usually correlated with more severe crack formation in the cathode, as observed in NCA[51] and NMC[52] materials, which leads to decreased electrochemical performance. The intrinsic

reason may be that fast charging and discharging process accompanies rapid volume change, which produces a strain that cannot be accommodated accordingly in a considerably short period. Our recent study[49] showed that higher cycling rate leads to dramatic increment of crack formation at the secondary particle level.

However, some researchers hold an opposite opinion that the crack formation is independent of fast charging and discharging. Zhao et al.[75] argued that the mechanical disintegration caused by fast charging was not obvious. They pointed out that higher cycling-rate could limit the total amount of Li ions inserted or extracted from the layered structure, which would reduce the volumetric change of the cathode and thus lower the disintegration extent of the secondary particles. Their observation of reduced R_{SEI} (Li ion transport resistance through the SEI) and R_{ct} for fast charging and discharging samples proved that less fresh surface was produced because of the lower extent of crack formation. Another example is that for NMC333, 0.1 C and 1 C made no difference to crack formation when the cell was cycled at a low cut-off voltage[38]. Furthermore, *in situ* acoustic emission experiments[60] showed that the C-rate independent crack formation is also valid in LCO. Therefore, these contradicting studies signify the need for more investigations to better understand the relationship between fast charging and crack formation.

Cycle numbers

It is believed that chemomechanical breakdown occurs only after long term cycling.[99,100] However, researchers have observed crack formation even after the first cycle[40,53]. The fracture and fragmentation evolutions in NCA materials[40] were successfully characterized using the SEM-focused ion beam (SEM-FIB) snapshot approach. Fig. 10 (a) to (d) show the same particle in the as prepared condition and after the first, second, and third

cycle. It is evident that the as prepared sample had an intact secondary particle, and the crack formation and intergrain separation occurred after the first cycle and increased as a function of cycle number. Furthermore, elastic modulus and hardness of NMC materials[98] showed the most dramatic reduction after the first cycle, and then they decreased gradually as a function of cycle numbers. This means most chemomechanical breakdown occurred during the first cycles, and afterwards cracks grew at a much slower speed. The mechanism behind such observation has not been proposed yet. Here, we propose a possible mechanism called "positive feedback effect". During the charging and discharging process, charge heterogeneity is induced by crack formation, as shown in Fig. 3 (d) and (e). The charge heterogeneity, in turn, induces more micro-strain, which can accelerate the crack formation process. Overall, more cracks promote higher extent of charge heterogeneity and higher extent of charge heterogeneity induces more micro-strain, which can accelerate the crack formation process. This positive feedback theory can explain that at the beginning of crack formation process, the strain was accumulating, and when the strain reached a specific level, the number of cracks would increase dramatically. Fig. 10 (e) shows that the length of cracks increased dramatically in the beginning and gradually afterwards. The former result is consistent with Carter's acoustic emission experiment (Fig. 10 (f))[60], which proved that crack formation increased dramatically in the middle of first charge cycle. The acoustic emission experiment also showed that crack formation was highly concentrated in the first charge cycle. The possible reason is that after the drastic crack formation process, large volume of cracks can accommodate the volume change of the cathodes. Complete understanding of the microstructural evolution at the early stage needs further investigation.

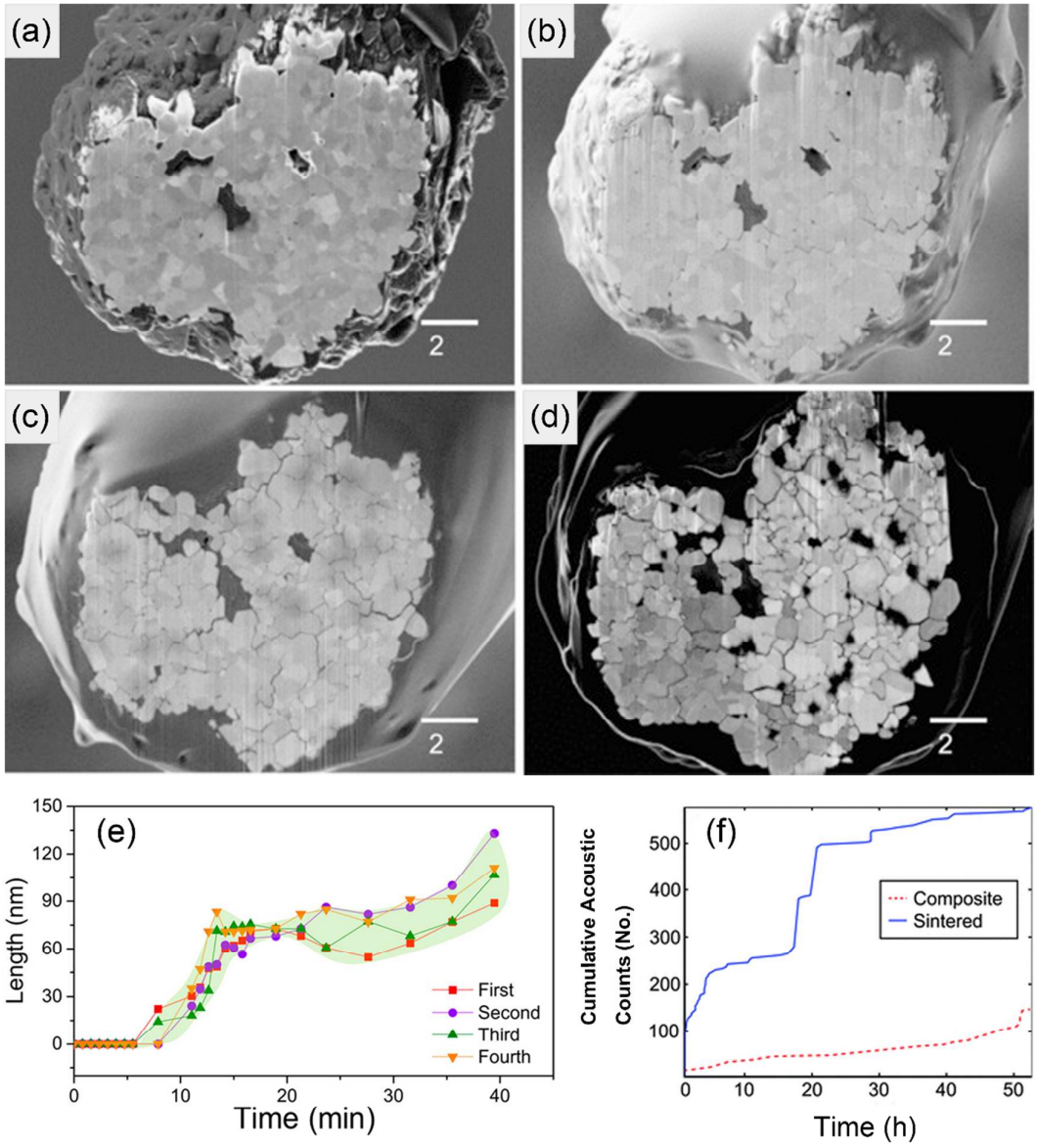

Fig. 10 (a-d) The evolution of particle fracture and fragmentation as a function of cycle numbers. These SEM-FIB snapshot images show the same particle in the (a) as-prepared condition and after the (b) first, (c) second, and (d) third cycle.[40] (e) The evolution of crack length for four independent cracks as a function of time under thermal abuse condition.[35] (f) Cumulative acoustic counts for sintered and thick composite pellet LCO electrodes during the

first charge at a C/50 rate.[101] Used with permission from ref. 40, 35, and 101.

3.3 Crack formation mechanisms

Evolution of crystal structures

During the electrochemical cycling processes, the lattice structure of LCMs experience periodic changes[54,92,102,103], which lead to micro-strain accumulation[104] and subsequent crack formation. The *in situ* synchrotron X-ray diffraction (XRD) patterns of NMC622 material in Fig. 11 (a) shows that the peak positions changed periodically and had high reversibility. The corresponding lattice parameters and unit cell volumes are shown in Fig. 11 (b) and (c), respectively. For H1 phase, the a, b, and c lattice parameters showed negligible changes. For H2 phase, as Li ions de-intercalated from the structure, the c lattice parameter first increased while a/b lattice parameter decreased. With more Li ions removed from the lattice (cur-off voltage higher than 4.2 V), the c axis contracted dramatically while a/b lattice parameter increased slightly. The calculated unit volumes are shown in Fig. 11 (c), and the volume change is about 4%, which proves that the bulk crystal structure is stable during electrochemical cycling processes. However, in the vicinity of the particle surface, after the removal of surface Li ions, transition metal ions could move to those vacant Li sites, which resulted in the phase transformation from layered (R-3m) to spinel (Fd-3m) and/or rock-salt (Fm-3m) phase.[79,105,106] The phase transformation process produce strains that can promote the formation of cracks. Other examples, such as LCO, also prove that phase transformation under high cut-off voltage accounts for structural instability and crack formation.[57] To conclude, evolution of crystal structure is one of the primary reasons for crack formation.

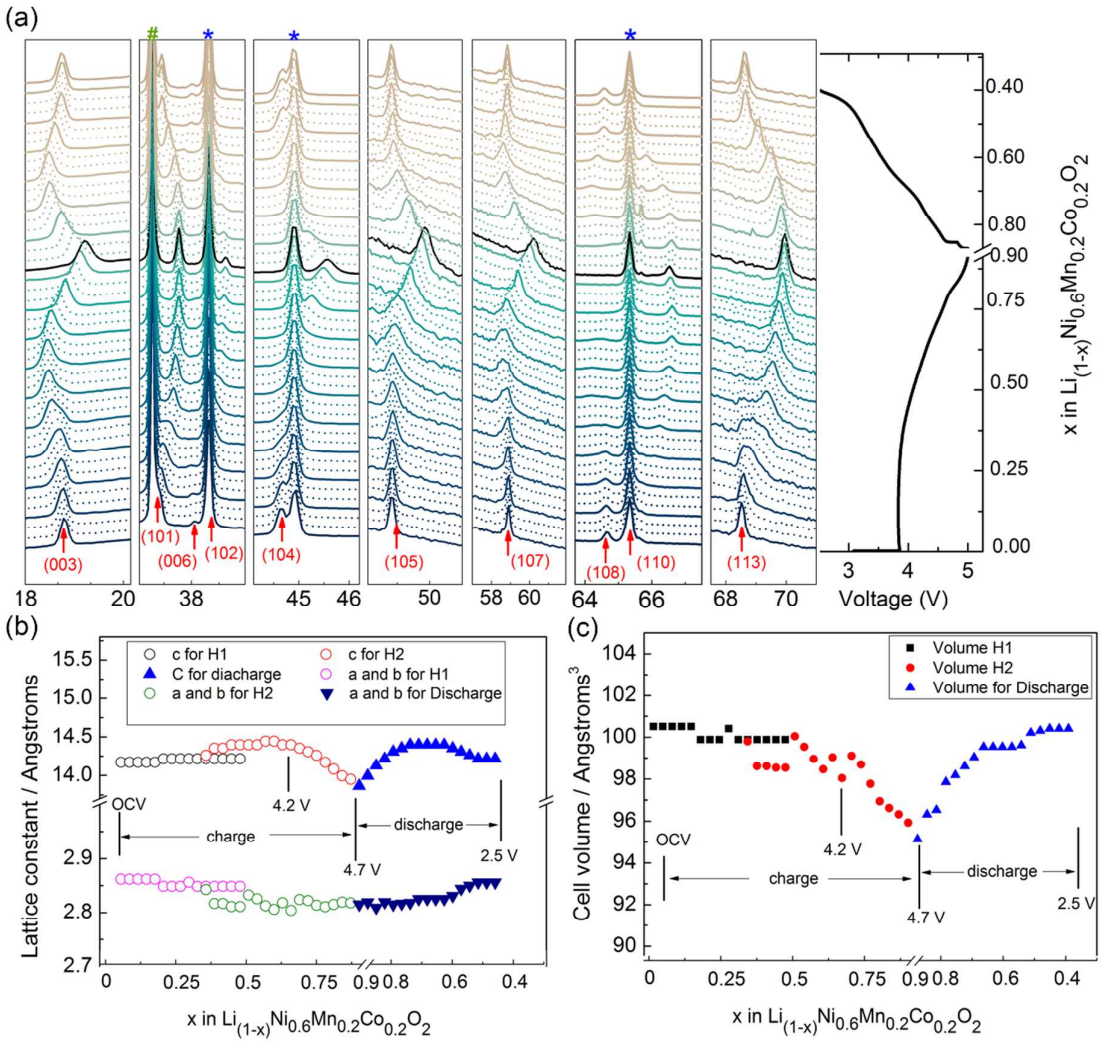

458

459 Fig. 11 (a) *In situ* synchrotron XRD patterns of NMC622 (cycled at C/10 between 2.5-4.7 V)
460 showing the periodic changes of crystal structure. The evolution of (b) a and c-axis parameters
461 and (c) the unit cell volume change of NMC as a function of charge/discharge depth during the
462 first cycle.[54] Used with permission from ref. 54.

463

464 **Propagation of dislocations**

465 Intragranular cracks have negative impacts such as lattice oxygen release, transition

metal and Li mixing, and rock-salt structure formation[70]. The nucleation and propagation of intragranular cracks is mostly related with dislocations. Primary particles have random orientations and they are densely packed. Processes such as electrochemical cycling and high temperature calcination can produce strains between primary particles. The induced strains cannot be consistently accommodated which leads to the generation of dislocations. The propagation of dislocation[38,64,96,107] can lead to the formation of two categories of intragranular cracks: premature intragranular cracks (pink arrows in Fig. 12 (a)) and mature intragranular cracks (yellow arrows in Fig. 12 (a)).[38] It is believed that the mature intragranular cracks are developed from the premature ones. The HAADF-STEM image in Fig. 12 (b) shows that the width of the premature cracks was about 0.72 nm, which was caused by the splitting of two neighboring transition metal slabs and propagating along the (003) planes. This observation explains how the intergranular cracks were predominantly parallel to (003) planes in the layered structure. Furthermore, the annular bright-field (ABF) STEM image in Fig. 12 (c) shows that the inter-slab between two transition metal layers was not empty, which proves that the premature cracks were formed by the loss of transition metal layer. The inserted circles in Fig. 12 (d) are the TEM images for the cathode particles cycled at different cut-off voltages. From Fig. 12 (d), the authors pointed out that the propagation of dislocation is an electrochemically activated process, because intragranular crack formation directly correlate with high voltage cycling. However, this argument might not be strong enough, since more Li ions can be extracted from the cathode material under high cut-off voltage condition, inducing more volume change and microstrain, which might also be responsible for the intragranular crack formation. Fig. 12 (e) is an overall scheme showing the intragranular crack evolution process: electrochemical and thermal process initiated the occurrence of dislocations, which then propagated along the transition metal layer direction

and formed intragranular cracks. Nevertheless, the actual formation mechanism is still not well understood and there are very few reports on the topic. Thus, more investigation is required for better understanding.

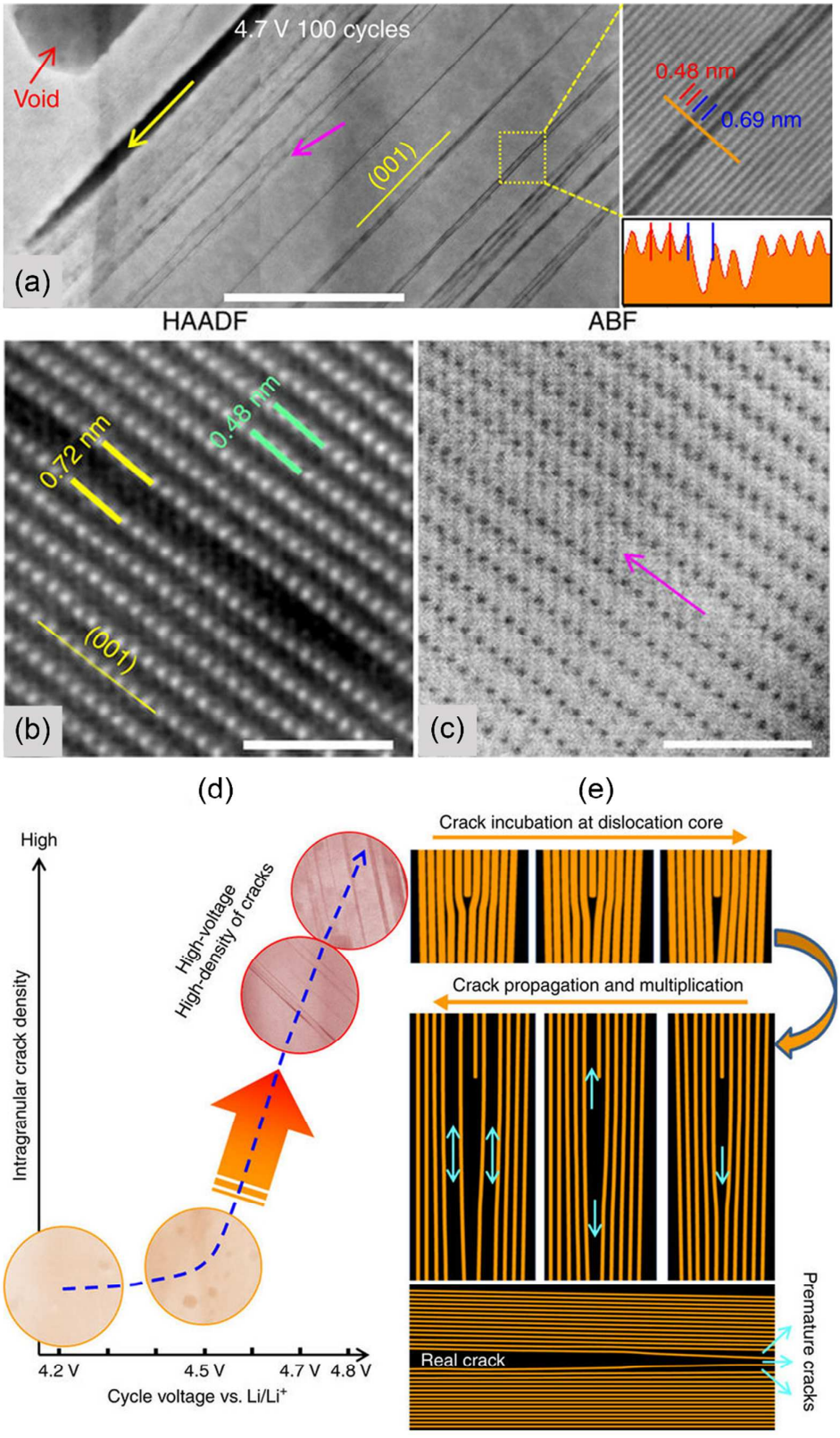
4.7 V 100 cycles
Void
(001)
0.48 nm
0.69 nm
(a)
HAADF
ABF
0.72 nm
0.48 nm
(001)
(b)
(c)
(d)
(e)
High
Intragranular crack density
High-voltage
High-density of cracks
4.2 V
4.5 V
4.7 V
4.8 V
Cycle voltage vs. Li/Li+
Crack incubation at dislocation core
Crack propagation and multiplication
Real crack
Premature cracks

493

Fig. 12 (a) Observation of the intragranular cracks along (001) plane in NMC333 cathode from HAADF images. The yellow arrows indicate mature cracks and the pink arrows indicate premature cracks. The scale bar is 50nm. The STEM images of the same premature cracks under (b) HAADF and (c) ABF mode. (d) The HAADF-STEM images showing that intragranular crack formation in NMC333 is governed by cut-off voltage. (e) Schematic illustration of the dislocation-assisted crack incubation, propagation and multiplication process.[38] Used with permission from ref. 38.

Lattice oxygen release

Lattice oxygen release from cathode material[35,70,108] also contributes to intragranular and intergranular crack formation since it is related with phase transformation (from the layered structure to spinel and/or rock-salt structure)[79] and strain accumulation[109]. Lattice oxygen release can be induced by overcharge of cathode material[110,111] or thermal abuse conditions[35]. Moreover, lattice oxygen release is not homogeneous[35,112] (Fig. 13 (a)) at the secondary particle level due to the different orientation-dependent oxygen release rate[106]. We observed inhomogeneous Ni valence state distribution at the secondary particle level, which is an indication that the oxygen release is also heterogeneous, since oxygen release are associated with the reduction of Ni due to the Ni3d-O2p hybridization[113,114]. The oxygen release induced strain, such as mismatch strain and shear stress, cannot be accommodated by the randomly orientated primary particles and it can be released through the formation of cracks along the weakest regions – grain boundaries (Fig. 13 (b)). Grain boundaries are the weakest regions since primary particles are randomly orientated and volume change is anisotropic. The intergranular crack formation can ultimately lead to the detachment of primary particles, as mentioned earlier in this paper. Furthermore, the oxygen vacancy

evolution showed that the surface is subjected to more oxygen loss and subsequently more volume change (Fig. 13 (c)). The induced tensile stress between the bulk and the surface further adds up to the grain boundary strain and initiate a radical intragranular crack from the bulk (Fig. 13 (d)), in addition to the observed intergranular crack.

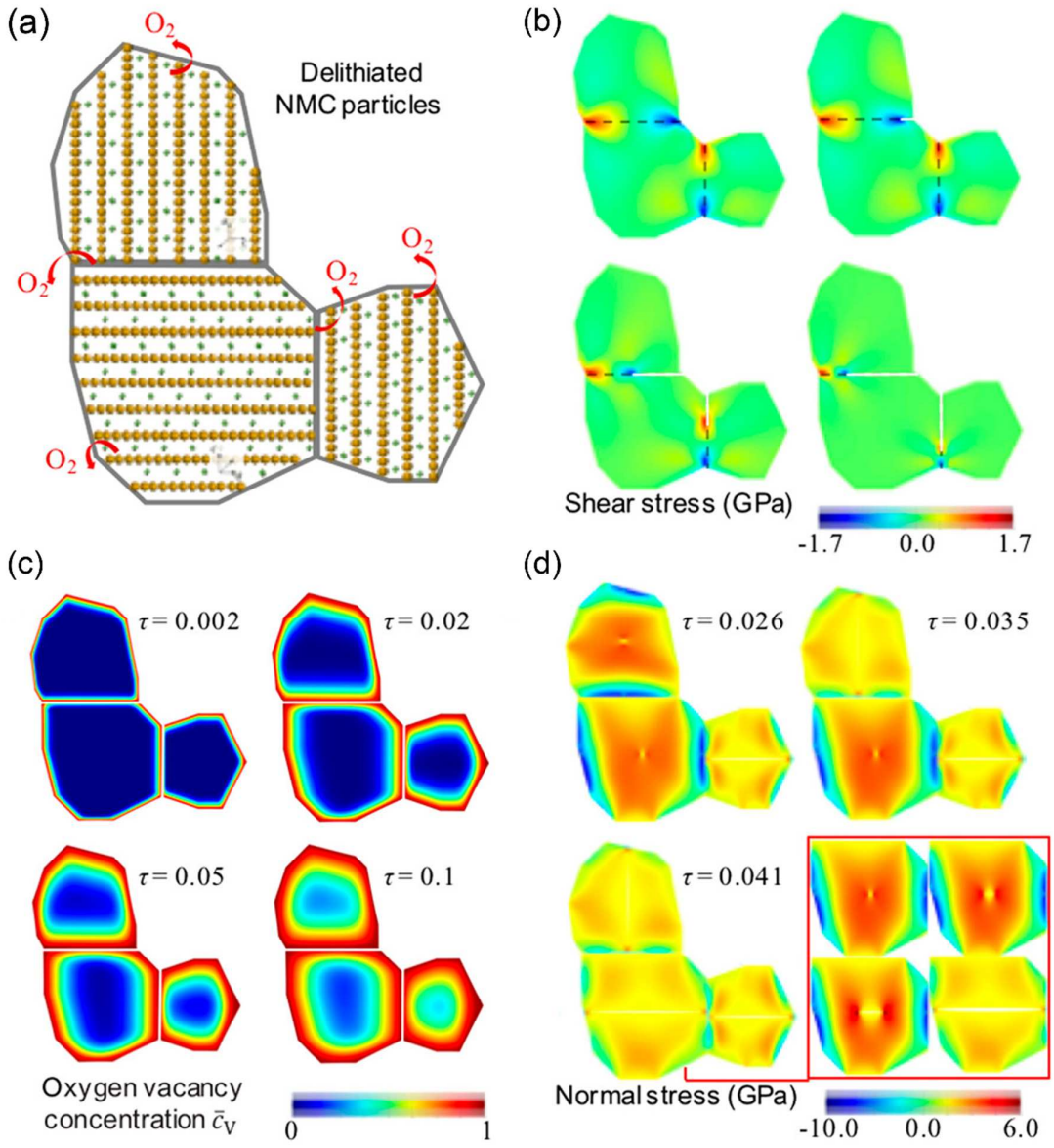

Fig. 13 (a) Finite element modeling (FEM) model of multiple randomly orientated NMC grains. (b) Phase transformation induced evolution of shear stress and formation of

intergranular cracks along the grain boundaries. (c) Surface and bulk oxygen vacancies distribution. (d) Oxygen release induced nucleation and propagation of intragranular cracks in NMC.[35] Used with permission from ref. 35.

Three main crack formation mechanisms are reviewed in this section. First, evolution of crystal structure produces strain in the cathode material because of the volume expansion/contraction. The accumulated strain is released through the formation of cracks. Second, the initiation of defects (e.g., dislocations) is inevitable and associated with the material synthesis process. The propogation of dislocations induces the formation of intragranular cracks. The growth of intragranular cracks can potentially lead to the formation of intergranular cracks. Third, oxygen release, which leads to the phase transformation and strain accumulation, can also promote the chemomechanical breakdown of LCMs. Here we emphasize that these crack formation mechanisms are not independent to each other. For example, evolution of crystal structure can produce strain that promotes the initiation of dislocations.

4. Ways to enhance the chemomechanical properties:

Chemomechanical breakdown of LCMs is thought to be one of the key reasons that lead to capacity fading of LIBs and it has been intensively observed. To date, there has been a limited number of reports that investigate how to enhance the chemomechanical properties of LCMs or reduce the negative effects of cracking. We summarized current methods that can either mitigate the crack formation or reduce the negative impacts of cracks.

Surface engineering

Surface engineering[115] can mitigate undesired cathode–electrolyte side reactions

549 and reduce surface crack formation. Two main mechanisms are proposed for the function of
550 the coating layer. The first mechanism behind coating is that the coating layer can work as a
551 barrier to electrolyte infiltration effect. Solid electrolyte Li_3PO_4 (LPO) coating to NMC
552 primary particles[68,116] was achieved by atomic layer deposition (ALD)[117] and low temperature
553 annealing (Fig. 14 (a))[116]. The solid electrolyte layer could prevent the electrolyte infiltration;
554 thus the extent of cathode–electrolyte reactions was reduced. The second mechanism behind
555 coating is that the coating layer works as an HF scavenger. HF is a strong acid and it can react
556 with LCMs which can lead to transition metal dissolution and electrolyte decomposition. By
557 consuming the hazardous HF, the undesired reaction between electrolyte and active cathode
558 material can thus be mitigated.[118,119,120] Methods that adopt the second mechanism include:
559 $MgAl_2O_4$ coating to LCO[121], Al_2O_3 coating to NMC[122,123,124], and $Co_3(PO_4)_2$ coating to
560 NCA[125] . The Al_2O_3 coating layer is chemically inactive to electrolyte and it works as a
561 protection layer for NMC material under high cut-off voltage (>4.4 V) condition, since it
562 mitigates the side reaction between the electrolyte and the highly active Ni sites.

563 A novel method, gradient structure design, can also be categorized as a surface
564 engineering method. Mn-rich NMC material is highly stable with low discharge capacity
565 since Mn is electrochemical inactive. Ni-rich NMC material, on the contrary, is low in
566 stability with high discharge capacity. A core-shell structure design of cathode material was
567 achieved with Mn-rich NMC as the shell and Ni-rich NMC as the core at the secondary
568 particle level (Fig. 14 (b))[126]. This design significantly improved the stability of NMC
569 materials. The core-shell structure was further developed to full concentration gradient
570 structure[127,128], in which the Ni-content decreased linearly and the Mn content increased
571 linearly from the core to the surface (Fig. 14 (c)). With the full concentration gradient
572 structure, the initial capacity of $LiNi_{0.75}Co_{0.10}Mn_{0.15}O_2$ could reach ~215 mAh/g with a

573 capacity retention of more than 90% after 1000 cycles at 1C. The primary reason for the
574 excellent performance is that the near surface region was stabilized with the Mn-rich NMC
575 material.

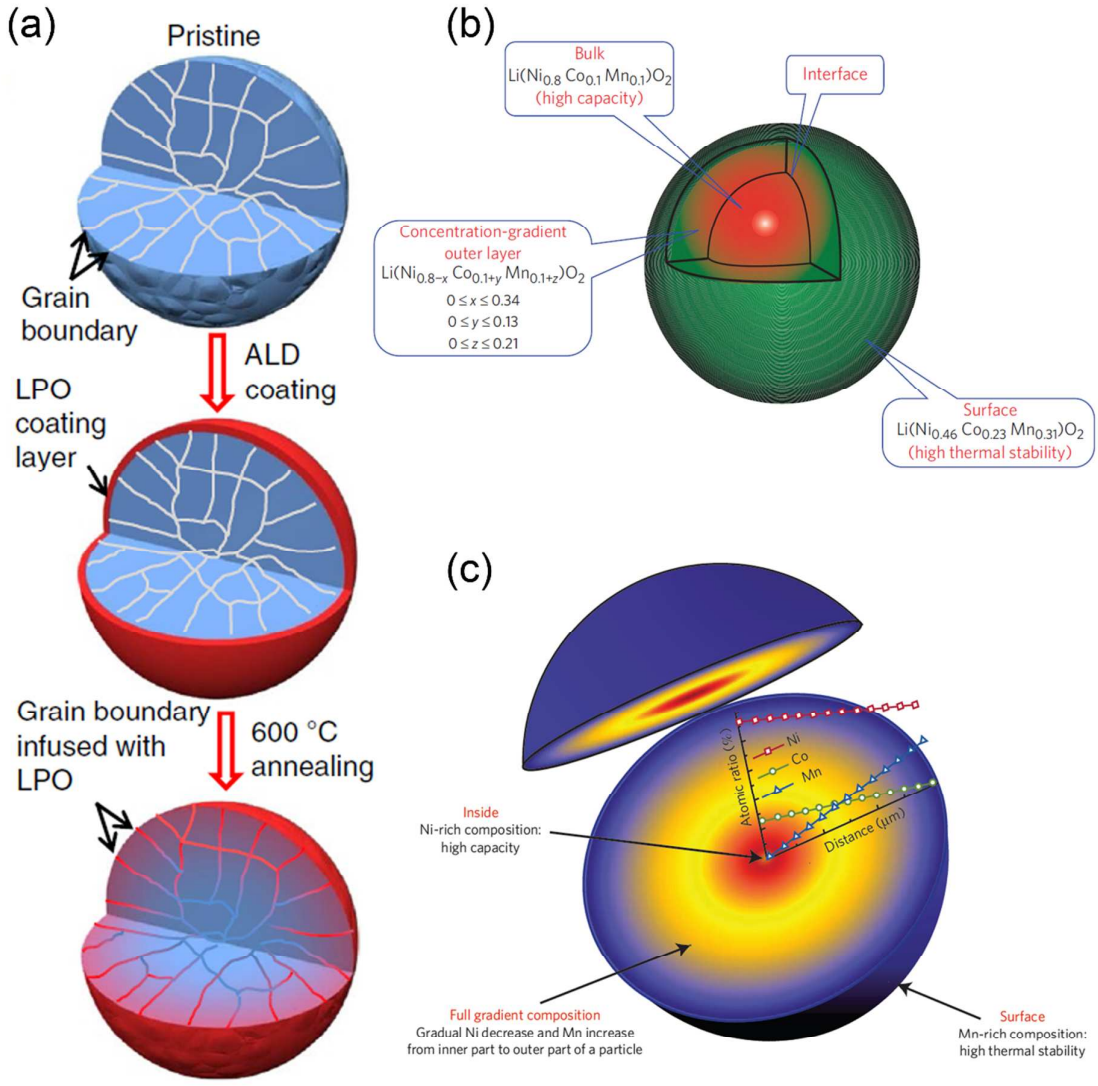

576

577 Fig. 14 (a) Synthetic procedure of LPO coated NMC. NMC particle is coated with LPO by
578 ALD, followed by annealing process.[55]. (b) Schematic diagram of NMC particle with Ni-rich
579 core and Mn-rich shell structure[126]. (c) Schematic diagram of NMC particle with full
580 concentration gradient structure. The Ni-content decreases linearly while Mn content

increases linearly from the bulk to the surface[127]. Used with permission from ref. 55, 126, and 127.

Grain engineering

In a secondary cathode particle, most primary particles are randomly orientated. During the electrochemical cycling process, anisotropic volume change induced microstrain cannot be concordantly accommodated, which initiates the formation of cracks. Sun and co-workers successfully enhanced the chemomechanical properties of cathode particles by grain engineering[56,129]. The grain engineering method is based on two-sloped full concentration gradient (TSFCG) design and rod-shaped primary particles. Cathode particles with the TSFCG design have two gradient slopes: from the core to near-surface region, the concentration gradients for each transition metal are smooth, whereas from the near-surface region to surface, the concentration gradients for transition metals change abruptly. The TSFCG design can be achieved with co-precipitation method by tuning the ratio of transition metals in the reagent.[130,131] In addition to the TSFCG design, another important feature of this advanced design is the columnar grains, which is formed by the rod-shaped primary particles[129]. Without grain engineering, primary particles have random orientations, which makes the secondary particle mechanically unstable (Fig. 15 (a-c)). Grain engineering significantly enhance the chemomechanical property of cathode material (Fig. 15 (d-f)). The underlying reason for the enhanced chemomechanical property is that the highly correlated particle orientation can reduce the anisotropic internal microstrain (Fig. 15 (g)).

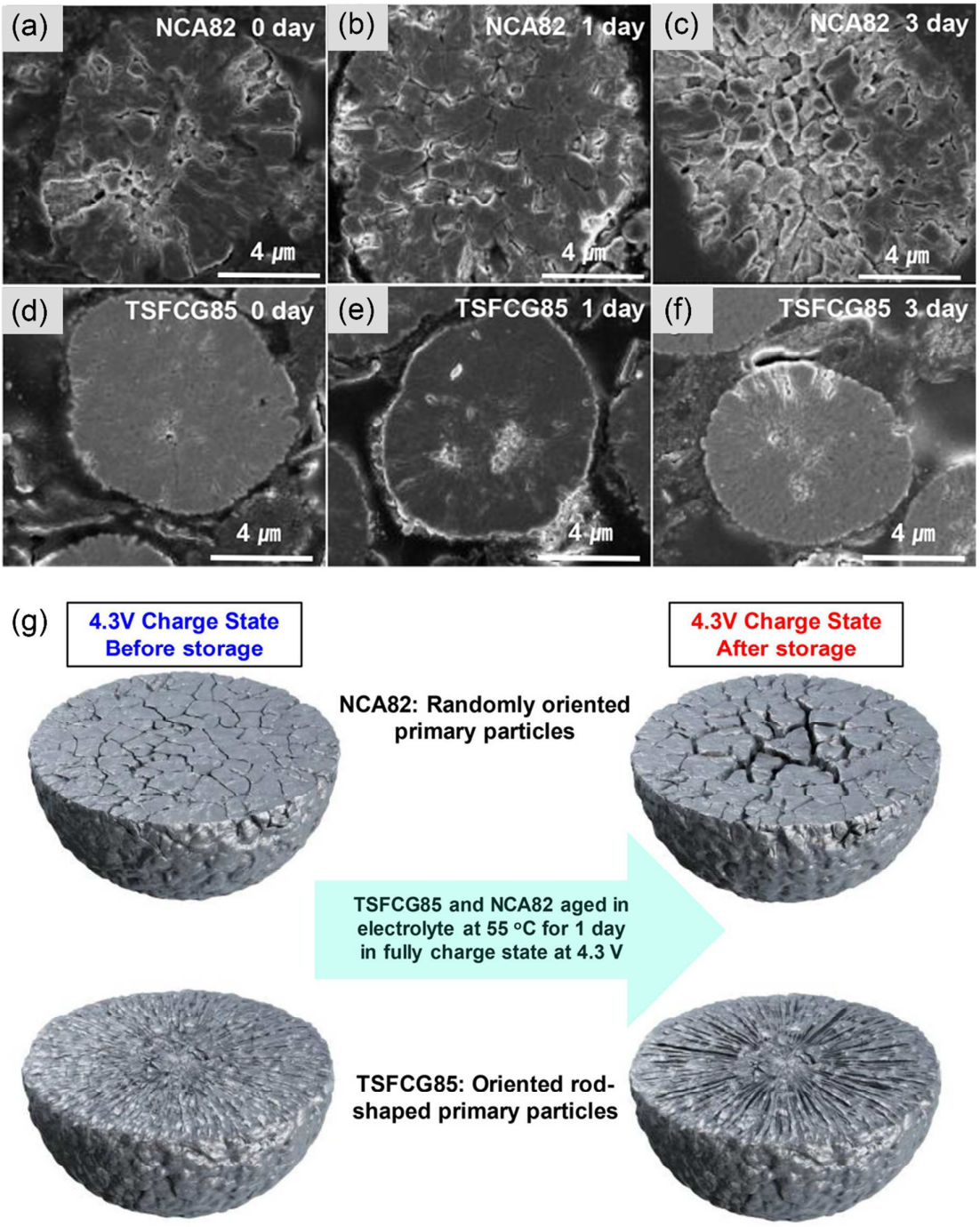

602

603 Fig. 15 (a-f) High-magnification cross-section SEM images of $LiNi_{0.82}Co_{0.14}Al_{0.04}O_2$ (NCA82)
604 and TSFCG-$LiNi_{0.85}Mn_{0.10}Co_{0.05}O_2$ (TSFCG85) cathode particles. All of the cathode were
605 charged to 4.3 V first, and then soaked in the electrolyte for different length of time.

606 Cross-section SEM images of the NCA82 cathode particles soaked in electrolyte for (a) 0 day,
607 (b) 1 day, and (c) 3 days. Dramatic crack formation were observed in the NCA82 particle.
608 Cross-section SEM images of the TSFCG85 cathode particles soaked in electrolyte for (d) 0
609 day, (e) 1 day, and (f) 3 days. No obvious crack formation were observed in TSFCG85
610 cathode particles. (g) Schematic representation of the NCA82 and TSFCG85 cathode
611 particles. After grain engineering, the uniformly orientated rod-shaped primary particles in
612 TSFCG85 can enhance the chemomechanical property.[129] Used with permission from ref.
613 129.

614 **Elemental substitution**

615 Elemental substitution, which is normally known as doping, has been intensively
616 investigated, and is an effective strategy to mitigate chemomechanical breakdown. The
617 underline reasons for improved chemomechanical property can be attributed to less phase
618 transformation and/or higher structural stability. La and Al co-doping to LCO was proposed
619 recently to reduce phase transformation.[57] The chemomechanical property of LCO was
620 improved by mitigating the order-disorder transition at low voltage and the H1-3 phase
621 transformation at high voltage. The rearrangement of Li vacancies was blocked by the Al^{3+},
622 which served as a fixed charge center due to its smaller size and higher charge over Co^{2+}.
623 Readers are referred to more reports on suppressing phase transformation by elemental
624 substitution: Na substitution at Li site in NMC[132], Al substitution at the Mn site in Li and Mn
625 rich material[133], K doping to Li rich material[134] and Zr doping to NMC622[135] and LNO[136].
626 Elemental substitution can also enhance the chemomechanical property of cathode material
627 by enhancing its structural stability. *In situ* synchrotron XRD measurements showed that Mg
628 substitution to NCA could mitigate the drastic c axis shrinkage, thus reducing crack formation
629 under high voltage.[137] The overall volume change after doping was considerably reduced

after elemental substitution. Some more reports are: Al doping to NMC[138] and Mo^{6+} doping to NMC333[139].

Pre-cycling treatment, reduced particle size, and electrolyte additive

Pre-cycling treatment means increasing the cut-off voltage from low to high, and an example is increasing the cut-off voltage from 4.5 V by 0.1 V every two cycles to 4.8 V. Pre-cycling method was shown to be effective in mitigating the formation of microcracks at the particle surface[58,59]. With pre-cycling treatment, the discharge capacity of $Li[Ni_{0.17}Li_{0.2}Co_{0.07}Mn_{0.56}]O_2$ after 50 cycles reached to 250 mAh/g, while the untreated one only delivered about 200 mAh/g. However, the physicochemical meaning of this pre-cycling method has not been understood yet.

Moreover, one can also tune the primary and/or secondary particle size to enhance its chemomechanical property. Chiang et al.[60] proposed that when the primary particle is under some specific size, the formation of cracks would be dramatically reduced. From our recent study[49], we know that small secondary particles are more robust. However, this comes with the cost of inferior tap density and larger surface area. Based on this information, it is recommended to reduce the primary particle size, and at the same time, find a balance between the secondary particle size and better electrochemical performance.

Electrolyte additive is another method to enhance the chemomechanical stability of cathode material. Some electrolyte additive can form a protective layer on the cathode, which can mitigate the undesired side reactions such as transition metal dissolution[140,141]. This underlying mechanism is similar to that of surface engineering. Moreover, electrolyte additive that works as artificial HF scavenger can be added[61] to prevent the HF attack on the cathode material. By limiting the presence of HF, chemomechanical breakdown of the

cathode can thus be limited. Furthermore, electrolyte additives may help eliminate the surface oxygen loss to effectively limit the intragranular cracks reported in our previous study[35].

Each of the aforementioned methods has its own advantages and disadvantages. Surface engineering is a good way to mitigate the side reactions between the cathode and liquid electrolyte, and thus the secondary particles are intact after long cycling. However, some surface engineering methods – such as ALD – can be expensive and have high requirements for precursors, which makes it not less appealing for industry scale material synthesis. We are aware of increasing efforts to improve the manufacturability of the ALD technique for batteries. Furthermore, some coating layers have low electronic conductivity, which can potentially reduce the cyclability of the cathode. Mechanistically, the exact functions of coating layers are still debatable. It is still unclear how the ion transport takes place across the layers. More studies are needed to address this fundamental question. The gradient structure design, a novel surface engineering method, on the contrary, is relatively cheap, easy to accomplish at large scale, and more importantly, has good electronic conductivity. Nevertheless, the gradient structure design also has its own drawback: the Mn-rich surface induces more Mn dissolution during the cycling process, which can be detrimental to the overall cell performance including the integrity of the SEI on the anode surface. Grain engineering can effectively enhance the chemomechanical properties of cathode materials, but the synthesis of rod-like primary particle can potentially lead to higher cost. Elemental substitution is easy to achieve and is widely used in battery materials chemistry. Certain elemental substitutions may improve the electronic properties of layered oxides. For example, they may improve the oxygen stability[142,143] and inhibit the oxygen release induced chemomechanical breakdown. In summary, we believe that combining the aforementioned methods may lead to dramatically enhanced chemomechanical properties.

5. Chemomechanical breakdown of Na-cathode materials

Na, being in the same alkaline group as Li, has similar electrochemistry as Li and SIBs is another type of the most promising energy storage devices for the future, based on the abundant Na resource and low cost[144,145]. Many Na cathode has been proposed in a very short time, and some examples are: O3 type $NaMnO_2$[146], $NaTiO_2$[147], and $Na_{0.9}[Cu_{0.22}Fe_{0.30}Mn_{0.48}]O_2$[148]; P2 type $Na_{0.5}[Ni_{0.23}Fe_{0.13}Mn_{0.63}]O_2$[149], $Na_{0.6}Co_{0.25}Fe_{0.25}Mn_{0.5}O_2$[150], and $Na_{2/3}Ni_{1/3}Mn_{2/3}O_2$[151]. Here we point out that the explanation of notation system of layered structure, such as O3 and P2 can be understood through Delmas's investigation[152].

Chemomechanical breakdown of Na-cathode materials has also been reported, and similar formation mechanism as that in LIBs has been proposed: cathode–electrolyte side reactions and evolution of crystal structures. $NaPF_6$, similar to its counterpart $LiPF_6$ in LIBs, leads to the inevitable formation of HF, which can give rise to undesired side reactions between the Na cathode and electrolyte. These side reactions will lead to the chemomechanical breakdown of the Na cathode, such as cracking and exfoliation[62]. Along with the investigations of chemomechanical breakdown, the concomitant investigations on cathode material stabilization against crack formation are also very significant. Some of such stabilization techniques including surface engineering, such as Al_2O_3 coating[151,153,] and Al_2O_3/multi-walled carbon nanotube hybrid networks[153], were proved to be an effective way to reduce those unwanted side reactions. The Na cathode also experience volume change due to the intercalation and de-intercalation of Na ions[63]. The volume change can produce strains that is hard to accommodate, which can be released by the formation of cracks. Some novel Na cathodes, such as $Na_3TiP_3O_9N$[154] and Na_2FeSiO_4[155] were proposed since they have

relative small volume change and negligible strain. Researchers in the Na cathode area are still exploring new material and ways to enhance the discharge capacity and stability, topics like chemomechanical breakdown of Na-cathodes materials need further investigation.

6. Analytical techniques to study chemomechanical properties

Chemomechanical breakdown of battery particles is considered as three-dimensional defects that involves complicated chemical and structural transformations at multiple length scales. These defects are delicate enough that it can be interrupted by the experimental operation. Therefore, the characterization of these defects requires a range of nondestructive and 3D sensitive analytical techniques. X-ray and electron microscopic techniques are suitable for visualizing cracks, which have been done extensively in the field[156,157]. Only very recently, the field has moved from the descriptive microscopic analysis to the quantitative determination of cracks[49]. As elaborated above, the outcome of crack formation can induce chemical and structural transformations that start from the crack surface and propagate into the subsurface. These processes are similar to the surface degradation in most cathode materials. The characterization of these processes is similar to any surface chemistry analysis in battery materials. Over the last few years, we have witnessed many new and improved techniques that are suitable for analyzing chemomechanical breakdowns. This review is by no means to cover all of these techniques, thus we selectively discuss the ones that are emerging and relatively unexplored by the broad battery community. Readers are recommended to refer to some of the recently published comprehensive review articles regarding advanced characterization of battery materials[158,159,160,161,162,163,164].

Electron microscopy (EM) represents one of the most popular techniques that are widely available in a standard academic laboratory. Many of the aforementioned studies

relied solely on EM. In general, EM can provide quick assessments of chemomechanical properties by directly visualizing the cracks. TEM and SEM are complementary to each other in terms of spatial resolution. The powerful structural analysis capability of electron diffraction and EELS can reveal the most relevant information about the local chemistry. However, battery materials, in particular LCMs, are usually electron beam sensitive[165]. Special attention is recommended when analyzing the delicate local chemistry in the vicinity of cracks. Fractured particles can be observed with TEM[5,11] and FIB-SEM [41].

Synchrotron X-ray based imaging techniques have experienced a rapid development period over the last few years. The associated imaging processing and data analysis, especially with the big data and machine learning approach, are capable of pinpointing some finer details that were possible in the past. Spectroscopy-based X-ray imaging, coupled with 3D reconstruction, allows for almost nondestructively visualizing the 3D chemical and morphological information.[166] With a single voxel of 30 nm*30 nm*30 nm, there are numerous spectra in a single battery particle, thus the data analysis can become enormous without a high-throughput analysis method. To overcome such challenge, Liu and coworkers[167] have developed a machine learning methodology to identify functionally important minority phases (e.g., metallic Co) in LCO battery particles after cycling. They achieved this with a dataset of over 10 million spectra collected from more than one hundred particles. This approach and the associated novel clustering algorithms opens up the door for analyzing the local chemistry with spatial resolution in the vicinity of cracks. They also enable the path towards decoupling local chemistry from the global chemistry. The TXM, with a similar spatial resolution to SEM, can probe the distribution of microcracks inside battery particles.

Recently, we studied the dependence of crack formation on the charging rate (Fig. 13). After being cycled for 50 cycles at different rates, active particles were collected from the electrodes and analyzed by TXM. We observed that the crack density increased with the increase of charging rate (Fig. 16 (a)). We then mathematically processed the tomography data and quantified the porosity and surface area of these particles, which increased as the crack density increased (Fig. 16 (b)). To the best of our knowledge, this was the first time that the chemomechanical breakdown was quantified three dimensionally. We believe that such a quantification is important to understand the impact of crack formation on the cathode–electrolyte interfacial chemistry. The increased surface area can potentially improve the infiltration of electrolytic solution in the active particles, but it also inevitably increases the likelihood of cathode–electrolyte interfacial side reactions, such as surface reconstruction, electrolyte oxidation, and metal dissolution. Furthermore, the formation of microcracks in individual active particles can interrupt the continuity of electron transport, as electrons can only travel through the solid but not in the microcracks (Fig. 16 (c)). As the charging rate increased, the travel distance for electrons from inside the particle to the surface got longer.

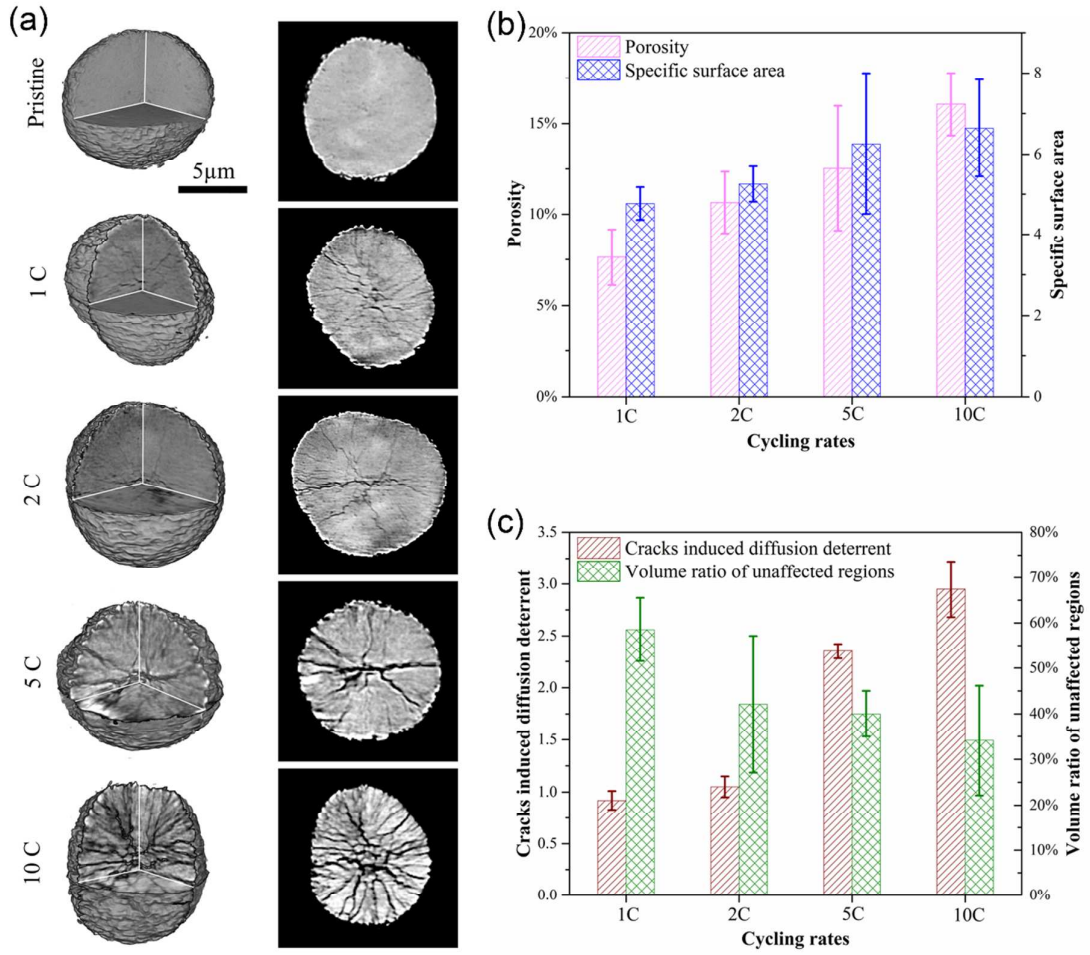

Fig. 16 Qualitatively and quantitatively characterization of cracks in NMC particles. (a) Reconstructed 3D and 2D particles from TXM data. The particles are at the as-prepared state and after 50 full cycles at 1 C, 2 C, 5 C and 10 C. The 2D slices are through the centers of the particles. Evolution of (b) the porosity and the specific crack surface area, (c) the crack induced diffusion deterrent and the unaffected regions as a function of cycling rates.[49] Used with permission from ref. 49.

In the earlier part of this review, we have discussed TXM for mapping the charge distribution in battery secondary particles and the method can be well integrated with the analysis of cracks. There is a complex interplay between internal stress and charge distribution. The heterogeneous distribution of internal stress can lead to non-uniform charge

distribution. On the other hand, the non-uniform charge distribution causes spatially dependent structural changes thus internal stress. The outcome of this interplay is the formation of microcracks. Further studies can combine the crack quantification with charge distribution mapping to establish the relationship between crack density and charge heterogeneity.

Although synchrotron X-ray spectroscopic imaging offers a powerful tool to study chemomechanical properties, it has a few drawbacks that need further development. First of all, the speed of data collection handicaps the *in situ* capability. Most X-ray spectroscopic imaging techniques need tens of minutes or even hours to complete a meaningful dataset for the area of interest. However, the chemomechanical processes are usually dynamic and take place at a small time scale. Therefore, *in situ* monitoring of cracks, especially their inception, is probably the next frontier. Second, the spatial resolution limits to only observing intergranular cracks for polycrystalline materials.

At the atomic scale, the formation and propagation of microcracks are mediated by the line defects such as dislocation. Some progress has been made in mapping dislocations inside battery particles (Fig. 17 (a-c))[64]. Bragg coherent diffraction imaging is a powerful tool in characterizing the edge dislocation displacement field. The evolution of dislocation lines under different charge states can then be built based on the displacement field[64]. Understanding the topological defects dynamics provides valuable information for future defect manipulation. In addition, studying the spatial distribution of strain dynamics in battery particles has been made possible (Fig. 17 (d))[65]. With knowledge on strain dynamics, we can further find the correlation between strain evolution and other factors, such as charge depth and chemical composition. The information from strain dynamic is also instructive for future material design.

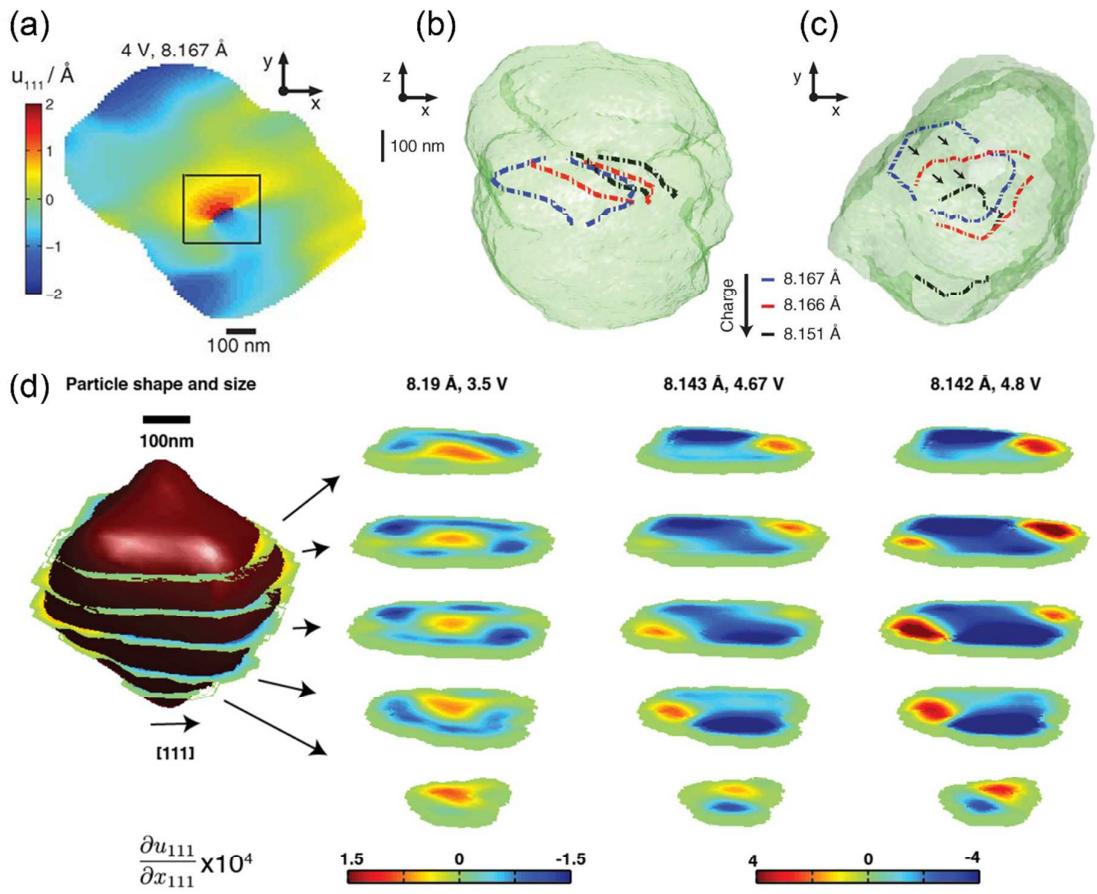

Fig. 17 (a-c) Topological defect evolution in a cathode particle under operando condition. (a) Displacement field for a cross section in a cathode particle. (b) Direct view of the edge dislocation line evolution under different charging states. (c) Direct view of the same edge dislocation line evolution as in (b) from a different direction.[64] (d) Evolution of the strain distribution inside a cathode particle under different charging conditions. Blue and red represent the α and β phases, respectively, for the cross sections at 8.143 and 8.142 Å.[65] Used with permission from ref. 64 and 65.

Moreover, many other state-of-the-art characterization methods are applied to study the structural evolution and mechanical properties. Neutron diffraction[168] has been applied to study the evolution of crystal structure. Nanoindentation[169,170,171] has been used to measure

the elastic, plastic, and fracture properties of cathode materials. All those aforementioned characterization methods provide significant insights into our future work.

7. Conclusions and perspectives

Alkali metal ion batteries have drawn much attention due to their current and future application in energy storage systems of different scales. However, chemomechanical breakdown of LCMs, which is partially responsible for the capacity fading in alkali metal ion batteries, remain unsolved. This review summarizes recent progress in characterizing, understanding, and modifying the chemomechanical behaviors of LCMs in alkali metal ion batteries. Details of the negative effects, impacting factors, formation mechanisms, modification methods, and characterization techniques of chemomechanical breakdown have been discussed in this review. Intragranular and intergranular cracks in LCMs can lead to poor electronic conductivity, loss of active material, more severe cathode–electrolyte side reactions, and higher extent of transition metal dissolution and SEI interruption. Intrinsic factors (Ni-content, primary and secondary particle size) and extrinsic factors (charge depth, charging and discharging rate, and cycle number) can affect the formation of cracks. Formation mechanisms of cracks, such as the evolution of crystal structure, propagation of dislocation, and oxygen release are addressed in detail. In addition, surface engineering, elemental substitution, pre-cycling treatment, reducing particle size, and electrolyte additive are good ways to mitigate the formation of cracks. Cracks in SIBs are also briefly covered in this review. Finally, light is brought onto the new analytical techniques that have been applied to the study of cracks.

The successful commercialization of LIBs has profoundly improved the quality of our lives in the past three decades. To make our society a sustainable one, large energy

storage system has imposed much stricter performance requisites on LIBs and SIBs. Therefore, chemomechanical breakdown of cathode materials, one of the main capacity fading mechanisms, must be restrained for higher performing LIBs and SIBs. Chemomechanical breakdown of layered oxides has been intensively observed, yet its formation mechanism remains vague.

The LCMs provide a good platform for the fundamental crystallography research because of the diverse phases transformation during electrochemical cycling. The LCMs, except LCO, are formed by randomly orientated single crystals. During charging/discharging process, LCMs experience nucleation and propagation of defects (e.g., dislocations). Better understanding these properties of the LCMs not only provides scientific insights into cracks formation but also further enriches our knowledge in crystallography. Moreover, the interplay between charge heterogeneity, compositional heterogeneity, and crack formation needs more studies. Understanding the formation mechanisms will give us valuable information regarding the next-generation advanced design principles. Based on current knowledge, reducing the primary particle size, surface engineering, and advanced nanostructure design are possible solutions. State-of-the-art techniques, such as TXM in combination with machine learning methodology, need further improvement on their spatial and temporal resolution to quantitatively study crack formation under practical operating conditions.

Conflicts of interest

There are no conflicts to declare.

Acknowledgements

The authors acknowledge support from the National Science Foundation under

Grant No. DMR-1832613. The work was also supported by the Department of Chemistry Startup at Virginia Tech. The authors acknowledge Yao Wang (Rice University, TX, USA) for her help in making figures.

References

1 J. Tollefson, *Nature*, 2008, **456**, 436–440.

2 M. Armand and J. M. Tarascon, *Nature*, 2008, **451**, 652–657.

3 V. Etacheri, R. Marom, R. Elazari, G. Salitra and D. Aurbach, *Energy Environ. Sci.*, 2011, **4**, 3243–3262.

4 R. R. Schaller, *IEEE Spectr.*, 1997, **34**, 52–59.

5 G. M. Joselin Herbert, S. Iniyan, E. Sreevalsan and S. Rajapandian, *Renew. Sustain. Energy Rev.*, 2007, **11**, 1117–1145.

6 S. Arnaltes and J. C. Burgos, 2006, **21**, 130–135.

7 G. K. Mor, O. K. Varghese, M. Paulose, K. Shankar and C. A. Grimes, *Sol. Energy Mater. Sol. Cells*, 2006, **90**, 2011–2075.

8 C. G. Granqvist, *Sol. Energy Mater. Sol. Cells*, 2007, **91**, 1529–1598.

9 G. W. Frey and D. M. Linke, *Energy Policy*, 2002, **30**, 1261–1265.

10 K. Srirangan, L. Akawi, M. Moo-Young and C. P. Chou, *Appl. Energy*, 2012, **100**, 172–186.

11 J. A. Ruiz, M. C. Juárez, M. P. Morales, P. Muñoz and M. A. Mendívil, *Renew. Sustain. Energy Rev.*, 2013, **18**, 174–183.

12 C. E. Reimers, L. M. Tender, S. Fertig and W. Wang, *Environ. Sci. Technol.*, 2001, **35**, 192–195.

13 J. M. Carrasco, L. G. Franquelo, J. T. Bialasiewicz, S. Member, E. Galván, R. C. P. Guisado, S. Member, M. Ángeles, M. Prats, J. I. León and N. Moreno-alfonso, *Ieee Trans. Ind. Electron.*, 2006, **53**, 1002–1016.

14 Z. Yang, J. Zhang, M. C. W. Kintner-Meyer, X. Lu, D. Choi, J. P. Lemmon and J. Liu, *Chem. Rev.*, 2011, **111**, 3577–3613.

15 S. Goriparti, E. Miele, F. De Angelis, E. Di Fabrizio, R. Proietti Zaccaria and C. Capiglia, *J. Power Sources*, 2014, **257**, 421–443.

16 M. T. McDowell, S. W. Lee, I. Ryu, H. Wu, W. D. Nix, J. W. Choi and Y. Cui, *Nano Lett.*, 2011, **11**, 4018–4025.

17 P. Poizot, S. Laruelle, S. Grugeon, L. Dupont and J. M. Tarascon, *Nature*, 2000, **407**, 496–499.

18 L. Q. Zhang, X. H. Liu, Y. Liu, S. Huang, T. Zhu, L. Gui, S. X. Mao, Z. Z. Ye, C. M. Wang, J. P. Sullivan and J. Y. Huang, *ACS Nano*, 2011, **5**, 4800–4809.

19 Y. Yao, M. T. McDowell, I. Ryu, H. Wu, N. Liu, L. Hu, W. D. Nix and Y. Cui, *Nano Lett.*, 2011, **11**, 2949–2954.

20 K. Zhao, M. Pharr, L. Hartle, J. J. Vlassak and Z. Suo, *J. Power Sources*, 2012, **218**, 6–14.

21 S. Zhang, K. Zhao, T. Zhu and J. Li, *Prog. Mater. Sci.*, 2017, **89**, 479–521.

22 R. Xu and K. Zhao, *J. Electrochem. Energy Convers. Storage*, 2016, **13**, 030803.

23 A. Mukhopadhyay and B. W. Sheldon, *Prog. Mater. Sci.*, 2014, **63**, 58–116.

24 Y. Jin, S. Li, A. Kushima, X. Zheng, Y. Sun, J. Xie, J. Sun, W. Xue, G. Zhou, J. Wu, F. Shi, R. Zhang, Z. Zhu, K. So, Y. Cui and J. Li, *Energy Environ. Sci.*, 2017, **10**, 580–592.

25 Y. Liu, D. Lin, P. Y. Yuen, K. Liu, J. Xie, R. H. Dauskardt and Y. Cui, *Adv. Mater.*,

2017, **29**, 1–8.

26 X. Xiao, P. Lu and D. Ahn, *Adv. Mater.*, 2011, **23**, 3911–3915.

27 Y. He, X. Yu, Y. Wang, H. Li and X. Huang, *Adv. Mater.*, 2011, **23**, 4938–4941.

28 Y. S. Hu, R. Demir-Cakan, M. M. Titirici, J. O. Müller, R. Schlögl, M. Antonietti and J. Maier, *Angew. Chemie - Int. Ed.*, 2008, **47**, 1645–1649.

29 M. S. Whittingham, *Chem. Rev.*, 2004, **104**, 4271–4301.

30 Z. Liu, A. Yu and J. Y. Lee, *J. Power Sources*, 1999, **81**–**82**, 416–419.

31 M. Yoshio, H. Noguchi, J. ichi Itoh, M. Okada and T. Mouri, *J. Power Sources*, 2000, **90**, 176–181.

32 M. D. Radin, S. Hy, M. Sina, C. Fang, H. Liu, J. Vinckeviciute, M. Zhang, M. S. Whittingham, Y. S. Meng and A. Van der Ven, *Adv. Energy Mater.*, 2017.

33 F. Lin, I. M. Markus, D. Nordlund, T.-C. Weng, M. D. Asta, H. L. Xin and M. M. Doeff, *Nat. Commun.*, 2014, **5**, 1–9.

34 K. Xu, *Chem. Rev.*, 2014, **114**, 11503–11618.

35 L. Mu, R. Lin, R. Xu, L. Han, S. Xia, D. Sokaras, J. Steiner, T.-C. Weng, D. Nordlund, M. M. Doeff, Y. Liu, K. Zhao, H. L. Xin and F. Lin, *Nano Lett.*, 2018, **18**, 3241–3249.

36 S.-K. Jung, H. Gwon, J. Hong, K.-Y. Park, D.-H. Seo, H. Kim, J. Hyun, W. Yang and K. Kang, *Adv. Energy Mater.*, 2014, **4**, 1300787.

37 N. P. W. Pieczonka, Z. Liu, P. Lu, K. L. Olson, J. Moote, B. R. Powell and J.-H. Kim, *J. Phys. Chem. C*, 2013, **117**, 15947–15957.

38 P. Yan, J. Zheng, M. Gu, J. Xiao, J. G. Zhang and C. M. Wang, *Nat. Commun.*, 2017, **8**, 1–9.

39 H. Liu, M. Wolf, K. Karki, Y. S. Yu, E. A. Stach, J. Cabana, K. W. Chapman and P. J. Chupas, *Nano Lett.*, 2017, **17**, 3452–3457.

40 D. J. Miller, C. Proff, J. G. Wen, D. P. Abraham and J. Bareño, *Adv. Energy Mater.*, 2013, **3**, 1098–1103.

41 H. H. Ryu, K. J. Park, C. S. Yoon and Y. K. Sun, *Chem. Mater.*, 2018, **30**, 1155–1163.

42 J. M. Lim, T. Hwang, D. Kim, M. S. Park, K. Cho and M. Cho, *Sci. Rep.*, 2017, **7**, 2–11.

43 K. Min and E. Cho, *Phys. Chem. Chem. Phys.*, 2017, **20**, 9045–9052.

44 H. H. Sun and A. Manthiram, *Chem. Mater.*, 2017, **29**, 8486–8493.

45 J. Zheng, M. Gu, J. Xiao, P. Zuo, C. Wang and J. G. Zhang, *Nano Lett.*, 2013, **13**, 3824–3830.

46 H. Zheng, Q. Sun, G. Liu, X. Song and V. S. Battaglia, *J. Power Sources*, 2012, **207**, 134–140.

47 D. R. Gallus, R. Schmitz, R. Wagner, B. Hoffmann, S. Nowak, I. Cekic-Laskovic, R. W. Schmitz and M. Winter, *Electrochim. Acta*, 2014, **134**, 393–398.

48 R. a. Fisher, M. R. Watt, W. Jud Ready, S. Il Cho, S. B. Lee, G. a. Snook, P. Kao, A. S. Best, G. Lota, K. Fic, E. Frackowiak, F. Béguin, M. D. Stoller, R. S. Ruoff, Arunabha Ghosg and Young Lee, O. Inganäs, S. Admassie, M. Vangari, T. Pryor, L. Jiang, J.-F. Lu, L. L. Wang, Q.-Y. Lai, H.-Y. Chu, Y. Zhao, G. Ćirić-Marjanovic, Y. Zhang, H. Feng, X. Wu, L. L. Wang, A. Zhang, T. Xia, H. Dong, X. Li, L. Zhang, T. H. Nguyen, A. Fraiwan, S. Choi, A. S. Aricò, P. Bruce, B. Scrosati, J. Tarascon, W. V. A. N. Schalkwijk, U. De Picardie, J. Verne, C. Umr-, G. Yu, X. Xie, L. Pan, Z. Bao, Y. Cui, L. Dong, Z. Chen, D. Yang and H. Lu, *Energy Environ. Sci.*, 2013, **3**, 4889–4899.

49 S. Xia, L. Mu, Z. Xu, J. Wang, C. Wei, L. Liu, P. Pianetta, K. Zhao, X. Yu, F. Lin and Y. Liu, .

50 C. S. Yoon, D.-W. Jun, S.-T. Myung and Y.-K. Sun, *ACS Energy Lett.*, 2017, **2**, 1150–

954 1155.
955 51 S. Watanabe, M. Kinoshita, T. Hosokawa, K. Morigaki and K. Nakura, *J. Power*
956 *Sources*, 2014, **258**, 210–217.
957 52 G. Li, Z. Zhang, Z. Huang, C. Yang, Z. Zuo and H. Zhou, *J. Solid State Electrochem.*,
958 2017, **21**, 673–682.
959 53 S. Zheng, R. Huang, Y. Makimura, Y. Ukyo, C. A. J. Fisher, T. Hirayama and Y.
960 Ikuhara, *J. Electrochem. Soc.*, 2011, **158**, A357.
961 54 C. Tian, D. Nordlund, H. L. Xin, Y. Xu, Y. Liu, D. Sokaras, F. Lin and M. M. Doeff, *J.*
962 *Electrochem. Soc.*, 2018, **165**, A696–A704.
963 55 P. Yan, J. Zheng, J. Liu, B. Wang, X. Cheng, Y. Zhang, X. Sun, C. Wang and J. Zhang,
964 *Nat. Energy*, 2018, **3**, 600–605.
965 56 H. J. Noh, Z. Chen, C. S. Yoon, J. Lu, K. Amine and Y. K. Sun, *Chem. Mater.*, 2013,
966 **25**, 2109–2115.
967 57 Q. Liu, X. Su, D. Lei, Y. Qin, J. Wen, F. Guo, Y. A. Wu, Y. Rong, R. Kou, X. Xiao, F.
968 Aguesse, J. Bareño, Y. Ren, W. Lu and Y. Li, *Nat. Energy*, ,
969 DOI:10.1038/s41560-018-0180-6.
970 58 A. Ito, D. Li, Y. Ohsawa and Y. Sato, *J. Power Sources*, 2008, **183**, 344–346.
971 59 A. Ito, D. Li, Y. Sato, M. Arao, M. Watanabe, M. Hatano, H. Horie and Y. Ohsawa, *J.*
972 *Power Sources*, 2010, **195**, 567–573.
973 60 W. H. Woodford, W. C. Carter and Y.-M. Chiang, *Energy Environ. Sci.*, 2012, **5**, 8014.
974 61 C. Peebles, R. Sahore, J. A. Gilbert, J. C. Garcia, A. Tornheim, J. Bareño, H. Iddir, C.
975 Liao and D. P. Abraham, *J. Electrochem. Soc.*, 2017, **164**, A1579–A1586.
976 62 J. Y. Hwang, S. T. Myung, C. S. Yoon, S. S. Kim, D. Aurbach and Y. K. Sun, *Adv.*
977 *Funct. Mater.*, 2016, **26**, 8083–8093.

63 L. Yang, X. Li, X. Ma, S. Xiong, P. Liu, Y. Tang, S. Cheng, Y. Y. Hu, M. Liu and H. Chen, *J. Power Sources*, 2018, **381**, 171–180.

64 U. Ulvestad, A. Singer, J. N. Clark, H. M. Cho, J. W. Kim, R. Harder, J. Maser, Y. S. Meng and O. G. Shpyrko, *Science (80-.).*, 2015, **348**, 1344–1347.

65 A. Ulvestad, A. Singer, H. M. Cho, J. N. Clark, R. Harder, J. Maser, Y. S. Meng and O. G. Shpyrko, *Nano Lett.*, 2014, **14**, 5123–5127.

66 M. Okubo, E. Hosono, J. Kim, M. Enomoto, N. Kojima, T. Kudo, H. Zhou and I. Honma, *J. Am. Chem. Soc.*, 2007, **129**, 7444–7452.

67 H. Wang, *J. Electrochem. Soc.*, 1999, **146**, 473.

68 H. Kim, M. G. Kim, H. Y. Jeong, H. Nam and J. Cho, *Nano Lett.*, 2015, **15**, 2111–2119.

69 G. Chen, X. Song and T. J. Richardson, *Electrochem. Solid-State Lett.*, 2006, **9**, A295.

70 P. Yan, J. Zheng, T. Chen, L. Luo, J. Zhang, S. Zhang and C. Wang, *Nat. Commun.*, 2018, 1–8.

71 N. Kiziltaş-Yavuz, M. Herklotz, A. M. Hashem, H. M. Abuzeid, B. Schwarz, H. Ehrenberg, A. Mauger and C. M. Julien, *Electrochim. Acta*, 2013, **113**, 313–321.

72 H. Gabrisch, J. Wilcox and M. M. Doeff, *Electrochem. Solid-State Lett.*, 2008, **11**, A25.

73 D. Wang, X. Wu, Z. Wang and L. Chen, *J. Power Sources*, 2005, **140**, 125–128.

74 A. V. Cresce, S. M. Russell, D. R. Baker, K. J. Gaskell and K. Xu, *Nano Lett.*, 2014, **14**, 1405–1412.

75 R. Xu, L. S. de Vasconcelos, J. Shi, J. Li and K. Zhao, *Exp. Mech.*, 2017, 1–11.

76 C. Tian, Y. Xu, D. Nordlund, F. Lin, J. Liu, Z. Sun, Y. Liu and M. Doeff, *Joule*, 2018, **2**, 464–477.

77 W. E. Gent, Y. Li, S. Ahn, J. Lim, Y. Liu, A. M. Wise, C. B. Gopal, D. N. Mueller, R. Davis, J. N. Weker, J. H. Park, S. K. Doo and W. C. Chueh, *Adv. Mater.*, 2016, 6631–6638.

78 B. Xu, C. R. Fell, M. Chi and Y. S. Meng, *Energy Environ. Sci.*, 2011, **4**, 2223.

79 A. Boulineau, L. Simonin, J. F. Colin, C. Bourbon and S. Patoux, *Nano Lett.*, 2013, **13**, 3857–3863.

80 M. Gu, I. Belharouak, J. Zheng, H. Wu, J. Xiao, A. Genc, K. Amine, S. Thevuthasan, D. R. Baer, J. G. Zhang, N. D. Browning, J. Liu and C. Wang, *ACS Nano*, 2013, **7**, 760–767.

81 Y. Xia, *J. Electrochem. Soc.*, 1996, **143**, 825.

82 J. Dong H, Y. J. Shin and S. M. Oh, *J. Electrochem. Soc.*, 1996, **143**, 2204–2211.

83 D. Aurbach, M. D. Levi, K. Gamulski, B. Markovsky, G. Salitra, E. Levi, U. Heider, L. Heider and R. Oesten, *J. Power Sources*, 1999, **81**–**82**, 472–479.

84 J. Vetter, P. Novák, M. R. Wagner, C. Veit, K. C. Möller, J. O. Besenhard, M. Winter, M. Wohlfahrt-Mehrens, C. Vogler and A. Hammouche, *J. Power Sources*, 2005, **147**, 269–281.

85 P. Arora, R. E. White and M. DOYLE, *J. Electrochem. Soc.*, 1998, **145**, 3647–3667.

86 D. Kim, S. Park, O. B. Chae, J. H. Ryu, Y.-U. Kim, R.-Z. Yin and S. M. Oh, *J. Electrochem. Soc.*, 2012, **159**, A193–A197.

87 W. K. Kim, D. W. Han, W. H. Ryu, S. J. Lim and H. S. Kwon, *Electrochim. Acta*, 2012, **71**, 17–21.

88 T. Joshi, K. Eom, G. Yushin and T. F. Fuller, *J. Electrochem. Soc.*, 2014, **161**, A1915–A1921.

89 Y. Bi, T. Wang, M. Liu, R. Du, W. Yang, Z. Liu, Z. Peng, Y. Liu, D. Wang and X. Sun,

RSC Adv., 2016, **6**, 19233–19237.

90 Y.-K. Sun, S.-W. Cho, S.-W. Lee, C. S. Yoon and K. Amine, *J. Electrochem. Soc.*, 2007, **154**, A168.

91 K. Min and E. Cho, *Phys. Chem. Chem. Phys.*, 2018, **20**, 9045–9052.

92 C. Liang, R. C. Longo, F. Kong, C. Zhang, Y. Nie, Y. Zheng and K. Cho, *ACS Appl. Mater. Interfaces*, , DOI:10.1021/acsami.7b17424.

93 J. Kim, H. Lee, H. Cha, M. Yoon, M. Park and J. Cho, *Adv. Energy Mater.*, 2018, **8**, 1–25.

94 A. Manthiram, J. C. Knight, S. T. Myung, S. M. Oh and Y. K. Sun, *Adv. Energy Mater.*, , DOI:10.1002/aenm.201501010.

95 E. C. Subbarao, *Colloids Surfaces A Physicochem. ...*, 1998, **113**, 3–11.

96 C. H. Shen, Q. Wang, H. J. Chen, C. G. Shi, H. Y. Zhang, L. Huang, J. T. Li and S. G. Sun, *ACS Appl. Mater. Interfaces*, 2016, **8**, 35323–35335.

97 H. J. Noh, S. Youn, C. S. Yoon and Y. K. Sun, *J. Power Sources*, 2013, **233**, 121–130.

98 R. Xu, H. Sun, L. S. de Vasconcelos and K. Zhao, *J. Electrochem. Soc.*, 2017, **164**, A3333–A3341.

99 N. Y. Kim, T. Yim, J. H. Song, J. S. Yu and Z. Lee, *J. Power Sources*, 2016, **307**, 641–648.

100 Y. Itou and Y. Ukyo, *J. Power Sources*, 2005, **146**, 39–44.

101 W. H. Woodford, W. C. Carter and Y. M. Chiang, *Energy Environ. Sci.*, 2012, **5**, 8014–8024.

102 R. Hausbrand, G. Cherkashinin, H. Ehrenberg, M. Gröting, K. Albe, C. Hess and W. Jaegermann, *Mater. Sci. Eng. B Solid-State Mater. Adv. Technol.*, 2015, **192**, 3–25.

103 A. O. Kondrakov, A. Schmidt, J. Xu, H. Geßwein, R. Mönig, P. Hartmann, H. Sommer,

T. Brezesinski and J. Janek, *J. Phys. Chem. C*, 2017, **121**, 3286–3294.

104 E. J. Lee, Z. Chen, H. J. Noh, S. C. Nam, S. Kang, D. H. Kim, K. Amine and Y. K. Sun, *Nano Lett.*, 2014, **14**, 4873–4880.

105 S.-K. Jung, H. Gwon, J. Hong, K.-Y. Park, D.-H. Seo, H. Kim, J. Hyun, W. Yang and K. Kang, *Adv. Energy Mater.*, 2014, **4**, 1300787.

106 F. Lin, D. Nordlund, T.-C. Weng, Y. Zhu, C. Ban, R. M. Richards and H. L. Xin, *Nat. Commun.*, , DOI:10.1038/ncomms4358.

107 H. Zhang, F. Omenya, P. Yan, L. Luo, M. S. Whittingham, C. Wang and G. Zhou, *ACS Energy Lett.*, 2017, **2**, 2607–2615.

108 R. Armstrong, M. Holzapfel, P. Novák, C. S. Johnson, S. H. Kang, M. M. Thackeray and P. G. Bruce, *J. Am. Chem. Soc.*, 2006, **128**, 8694–8698.

109 S. B. Adler, *J. Am. Ceram. Soc.*, 2004, **84**, 2117–2119.

110 J. H. Seo, J. Park, G. Plett and A. M. Sastry, *Electrochem. Solid-State Lett.*, 2010, **13**, A135.

111 V. Yurkiv, S. Sharifi-Asl, A. Ramasubramanian, R. Shahbazian-Yassar and F. Mashayek, *Comput. Mater. Sci.*, 2017, **140**, 299–306.

112 L. Mu, Q. Yuan, C. Tian, C. Wei, K. Zhang, J. Liu, M. M. Doeff, Y. Liu and F. Lin, *Nat. Commun.*, 1–8.

113 F. Lin, D. Nordlund, I. M. Markus, T. C. Weng, H. L. Xin and M. M. Doeff, *Energy Environ. Sci.*, 2014, **7**, 3077–3085.

114 S. Kuppan, Y. Xu, Y. Liu and G. Chen, *Nat. Commun.*, , DOI:10.1038/ncomms14309.

115 A. T. Appapillai, A. N. Mansour, J. Cho and Y. Shao-Horn, *Chem. Mater.*, 2007, **19**, 5748–5757.

116 P. Yan, J. Zheng, J. Liu, B. Wang, X. Cheng, Y. Zhang, X. Sun, C. Wang and J. Zhang,

Nat. Energy, , DOI:10.1038/s41560-018-0191-3.

117 X. Li, J. Liu, M. N. Banis, A. Lushington, R. Li, M. Cai and X. Sun, *Energy Environ. Sci.*, 2014, **7**, 768–778.

118 S. T. Myung, K. Amine and Y. K. Sun, *J. Mater. Chem.*, 2010, **20**, 7074–7095.

119 L. J. Fu, H. Liu, C. Li, Y. P. Wu, E. Rahm, R. Holze and H. Q. Wu, *Solid State Sci.*, 2006, **8**, 113–128.

120 Z. Chen, Y. Qin, K. Amine and Y. K. Sun, *J. Mater. Chem.*, 2010, **20**, 7606–7612.

121 G. T. K. Fey, Z. F. Wang, C. Z. Lu and T. P. Kumar, *J. Power Sources*, 2005, **146**, 245–249.

122 A. M. Wise, C. Ban, J. N. Weker, S. Misra, A. S. Cavanagh, Z. Wu, Z. Li, M. S. Whittingham, K. Xu, S. M. George and M. F. Toney, *Chem. Mater.*, 2015, **27**, 6146–6154.

123 B. Han, T. Paulauskas, B. Key, C. Peebles, J. S. Park, R. F. Klie, J. T. Vaughey and F. Dogan, *ACS Appl. Mater. Interfaces*, 2017, **9**, 14769–14778.

124 F. Dogan, J. T. Vaughey, H. Iddir and B. Key, *ACS Appl. Mater. Interfaces*, 2016, **8**, 16708–16717.

125 K. S. Ryu, S. H. Lee, B. K. Koo, J. W. Lee, K. M. Kim and Y. J. Park, *J. Appl. Electrochem.*, 2008, **38**, 1385–1390.

126 Y. K. Sun, S. T. Myung, B. C. Park, J. Prakash, I. Belharouak and K. Amine, *Nat. Mater.*, 2009, **8**, 320–324.

127 Y. K. Sun, Z. Chen, H. J. Noh, D. J. Lee, H. G. Jung, Y. Ren, S. Wang, C. S. Yoon, S. T. Myung and K. Amine, *Nat. Mater.*, 2012, **11**, 942–947.

128 U. H. Kim, E. J. Lee, C. S. Yoon, S. T. Myung and Y. K. Sun, *Adv. Energy Mater.*, 2016, **6**, 1–8.

129 C. S. Yoon, K. J. Park, U. H. Kim, K. H. Kang, H. H. Ryu and Y. K. Sun, *Chem. Mater.*, 2017, **29**, 10436–10445.

130 B. B. Lim, S. J. Yoon, K. J. Park, C. S. Yoon, S. J. Kim, J. J. Lee and Y. K. Sun, *Adv. Funct. Mater.*, 2015, **25**, 4673–4680.

131 J. H. Lee, C. S. Yoon, J.-Y. Hwang, S.-J. Kim, F. Maglia, P. Lamp, S.-T. Myung and Y.-K. Sun, *Energy Environ. Sci.*, 2016, **9**, 2152–2158.

132 M. N. Ates, Q. Jia, A. Shah, A. Busnaina, S. Mukerjee and K. M. Abraham, *J. Electrochem. Soc.*, 2013, **161**, A290–A301.

133 P. K. Nayak, J. Grinblat, M. Levi, E. Levi, S. Kim, J. W. Choi and D. Aurbach, *Adv. Energy Mater.*, 2016, **6**, 1–13.

134 Q. Li, G. Li, C. Fu, D. Luo, J. Fan and L. Li, *ACS Appl. Mater. Interfaces*, 2014, **6**, 10330–10341.

135 F. Schipper, M. Dixit, D. Kovacheva, M. Talianker, O. Haik, J. Grinblat, E. M. Erickson, C. Ghanty, D. T. Major, B. Markovsky and D. Aurbach, *J. Mater. Chem. A*, 2016, **4**, 16073–16084.

136 C. S. Yoon, U. Kim, G. Park, J. Kim, K. Kim, J. Kim and Y. Sun, 2018, **3**, 1634–1639.

137 T. Sasaki, V. Godbole, Y. Takeuchi, Y. Ukyo and P. Novák, *J. Electrochem. Soc.*, 2011, **158**, A1214.

138 U.-H. Kim, S.-T. Myung, C. S. Yoon and Y.-K. Sun, *ACS Energy Lett.*, 2017, 1848–1854.

139 S. H. Park, S. W. Oh and Y. K. Sun, *J. Power Sources*, 2005, **146**, 622–625.

140 S. S. Zhang, *J. Power Sources*, 2006, **162**, 1379–1394.

141 N. S. Choi, J. G. Han, S. Y. Ha, I. Park and C. K. Back, *RSC Adv.*, 2015, **5**, 2732–2748.

142 I. M. Markus, F. Lin, K. C. Kam, M. Asta and M. M. Doeff, *J. Phys. Chem. Lett.*, 2014,

5, 3649–3655.

143 S. Wolff-Goodrich, F. Lin, I. M. Markus, D. Nordlund, H. L. Xin, M. Asta and M. M. Doeff, *Phys. Chem. Chem. Phys.*, 2015, **17**, 21778–21781.

144 M. D. Slater, D. Kim, E. Lee and C. S. Johnson, *Adv. Funct. Mater.*, 2013, **23**, 947–958.

145 M. M. Rahman, Y. Xu, H. Cheng, Q. Shi, R. Kou, L. Mu, Q. Liu, S. Xia, X. Xiao, C. Sun, D. Sokaras, D. Nordlund, J. Zheng, Y. Liu and F. Lin, *Energy Environ. Sci.*, , DOI:10.1039/C8EE00309B.

146 X. Ma, H. Chen and G. Ceder, *J. Electrochem. Soc.*, 2011, **158**, A1307.

147 D. Wu, X. Li, B. Xu, N. Twu, L. Liu and G. Ceder, *Energy Environ. Sci.*, 2015, **8**, 195–202.

148 L. Mu, S. Xu, Y. Li, Y. S. Hu, H. Li, L. Chen and X. Huang, *Adv. Mater.*, 2015, **27**, 6928–6933.

149 I. Hasa, D. Buchholz, S. Passerini, B. Scrosati and J. Hassoun, *Adv. Energy Mater.*, 2014, **4**, 1400083.

150 L. Liu, X. Li, S. H. Bo, Y. Wang, H. Chen, N. Twu, D. Wu and G. Ceder, *Adv. Energy Mater.*, 2015, **5**, 1–5.

151 Y. Liu, X. Fang, A. Zhang, C. Shen, Q. Liu, H. A. Enaya and C. Zhou, *Nano Energy*, 2016, **27**, 27–34.

152 C. Delmas, C. Fouassier and P. Hagenmuller, *Phys. B+C*, 1980, **99**, 81–85.

153 J. H. Park, K. Park, R. H. Kim, D. J. Yun, S. Y. Park, D. Han, S. S. Lee and J. H. Park, *J. Mater. Chem. A*, 2015, **3**, 10730–10737.

154 J. Liu, D. Chang, P. Whitfield, Y. Janssen, X. Yu, Y. Zhou, J. Bai, J. Ko, K. W. Nam, L. Wu, Y. Zhu, M. Feygenson, G. Amatucci, A. Van Der Ven, X. Q. Yang and P. Khalifah,

Chem. Mater., 2014, **26**, 3295–3305.

155 S. Li, J. Guo, Z. Ye, X. Zhao, S. Wu, J.-X. Mi, C.-Z. Wang, Z. Gong, M. J. McDonald, Z. Zhu, K.-M. Ho and Y. Yang, *ACS Appl. Mater. Interfaces*, 2016, **8**, 17233–17238.

156 X. H. Liu, Y. Liu, A. Kushima, S. Zhang, T. Zhu, J. Li and J. Y. Huang, *Adv. Energy Mater.*, 2012, **2**, 722–741.

157 S. Watanabe, M. Kinoshita, T. Hosokawa, K. Morigaki and K. Nakura, *J. Power Sources*, 2014, **260**, 50–56.

158 F. Lin, Y. Liu, X. Yu, L. Cheng, A. Singer, O. G. Shpyrko, H. L. Xin, N. Tamura, C. Tian, T. C. Weng, X. Q. Yang, Y. S. Meng, D. Nordlund, W. Yang and M. M. Doeff, *Chem. Rev.*, 2017, **117**, 13123–13186.

159 W. Li, M. Li, Y. Hu, J. Lu, A. Lushington, R. Li, T. Wu, T.-K. Sham and X. Sun, *Small Methods*, 2018, **1700341**, 1700341.

160 C. Wei, S. Xia, H. Huang, Y. Mao, P. Pianetta and Y. Liu, *Acc. Chem. Res.*, , DOI:10.1021/acs.accounts.8b00123.

161 E. Zhao, K. Nie, X. Yu, Y. S. Hu, F. Wang, J. Xiao, H. Li and X. Huang, *Adv. Funct. Mater.*, 2018, **1707543**, 1–21.

162 W. Yang and T. P. Devereaux, *J. Power Sources*, 2018, **389**, 188–197.

163 Z. Shadike, E. Zhao, Y. N. Zhou, X. Yu, Y. Yang, E. Hu, S. Bak, L. Gu and X. Q. Yang, *Adv. Energy Mater.*, 2018, **1702588**, 1–29.

164 J. Lu, T. Wu and K. Amine, *Nat. Energy*, , DOI:10.1038/nenergy.2017.11.

165 F. Lin, I. M. Markus, M. M. Doeff and H. L. Xin, *Sci. Rep.*, 2014, **4**, 1–6.

166 F. Yang, Y. Liu, S. K. Martha, Z. Wu, J. C. Andrews, G. E. Ice, P. Pianetta and J. Nanda, *Nano Lett.*, , DOI:10.1021/nl502090z.

167 Y. Xu, E. Hu, K. Zhang, X. Wang, V. Borzenets, Z. Sun, P. Pianetta, X. Yu, Y. Liu, X.

Q. Yang and H. Li, *ACS Energy Lett.*, 2017, **2**, 1240–1245.

168 O. Dolotko, A. Senyshyn, M. J. Mühlbauer, K. Nikolowski and H. Ehrenberg, *J. Power Sources*, 2014, **255**, 197–203.

169 M. Qu, W. H. Woodford, J. M. Maloney, W. C. Carter, Y. M. Chiang and K. J. Van Vliet, *Adv. Energy Mater.*, 2012, **2**, 940–944.

170 L. S. de Vasconcelos, R. Xu, J. Li and K. Zhao, *Extrem. Mech. Lett.*, 2016, **9**, 495–502.

171 D. Kim, H. C. Shim, T. G. Yun, S. Hyun and S. M. Han, *Extrem. Mech. Lett.*, 2016, **9**, 439–448.

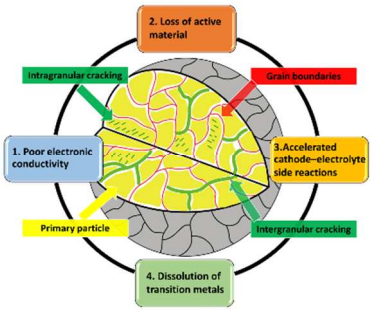

This review summarizes the recent progress in characterizing, understanding, and modifying the chemomechanical properties of layered oxide cathode materials.